



HAL
open science

Assessment of the oxygen reactivity in a gas storage facility by multiphase reactive transport modeling of field data for air injection into a sandstone reservoir in the Paris Basin, France

Irina Sin, Laurent de Windt, Camille Banc, Patrick Goblet, David Dequidt

► **To cite this version:**

Irina Sin, Laurent de Windt, Camille Banc, Patrick Goblet, David Dequidt. Assessment of the oxygen reactivity in a gas storage facility by multiphase reactive transport modeling of field data for air injection into a sandstone reservoir in the Paris Basin, France. *Science of the Total Environment*, 2023, 869, pp.161657. 10.1016/j.scitotenv.2023.161657 . hal-03981532

HAL Id: hal-03981532

<https://minesparis-psl.hal.science/hal-03981532>

Submitted on 9 Feb 2023

HAL is a multi-disciplinary open access archive for the deposit and dissemination of scientific research documents, whether they are published or not. The documents may come from teaching and research institutions in France or abroad, or from public or private research centers.

L'archive ouverte pluridisciplinaire **HAL**, est destinée au dépôt et à la diffusion de documents scientifiques de niveau recherche, publiés ou non, émanant des établissements d'enseignement et de recherche français ou étrangers, des laboratoires publics ou privés.



Assessment of the oxygen reactivity in a gas storage facility by multiphase reactive transport modeling of field data for air injection into a sandstone reservoir in the Paris Basin, France

Irina Sin^{a,*}, Laurent De Windt^a, Camille Banc^a, Patrick Goblet^a, David Dequidt^b

^a Mines Paris, PSL University, Center for Geosciences and Geoengineering, 35 rue Saint-Honoré, F-77305 Fontainebleau Cedex, France

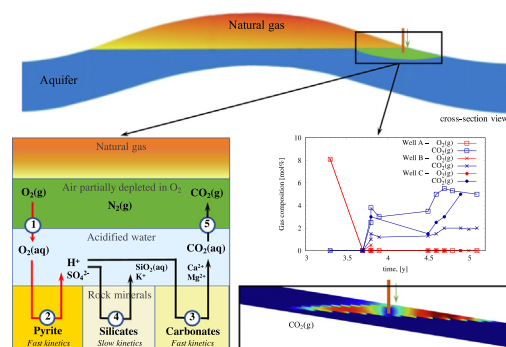
^b STORENGY–Geosciences Department, Bois-Colombes, France



HIGHLIGHTS

- 10 year field data show effects of injecting air with 8 % O₂ into aquifer gas storage.
- Data were modeled by multiphase reactive transport from batch to reservoir scales.
- The Damköhler number derived for O₂ reactivity and pyrite kinetics explains gas changes.
- Results are relevant for biomethane, CO₂ and compressed air storage facilities.

GRAPHICAL ABSTRACT



ARTICLE INFO

Editor: Jurgen Mahlknecht

Keywords:

Oxygen reactivity
Multiphase reactive transport
Underground gas storage
Biomethane
CAES
HYTEC

ABSTRACT

The first objective of this study is to present unique field data on a three-year pilot test during which air containing 8 mol% O₂(g) was injected as a cushion gas into a natural gas reservoir, a carbonate-cemented sandstone aquifer located in the Paris Basin (France). 10-year system survey showed that: the oxygen was fully depleted several months after injection completion, meanwhile CO₂(g) was detected around 2–6 mol%; the pH decreased from 8 to 6, while reducing conditions shifted to mildly oxidizing ones with increasing concentration of sulfates in equilibrium with gypsum. 3 years after injection completion, the pH gradually returned to its near initial state and sulfates were reduced by 2 to 3 times. The second objective is to develop a multiphase reactive transport model based on the field data. Simulations were constructed using the HYTEC reactive transport code, progressing from 0D-batch to 2D-reservoir configurations. The model reproduced the gas-water-rock reactive sequence: 1/ full depletion of the injected O₂(g) due to pyrite oxidation, 2/ leading to acidity production and dissolved sulfates, 3/ acidity buffering by calcite dissolution, 4/ followed by gypsum precipitation and CO₂(g) exsolution. The model demonstrated that pyrite kinetics was the most significant factor governing not only the amount of O₂(g), CO₂(g) and dissolved minerals, but also the spatial extent of these chemical reactions and, hence, the gas spread inside the reservoir. The formulated advective Damköhler number for oxygen consumption indicated advection- and reaction-dominant regimes explaining the gas composition and extension. The developed field-based model could be used as a workflow for other gas storage facilities, e.g. biomethane, compressed air, and CO₂. For underground biomethane storage, the O₂(g) contents recommended in Europe, i.e. the EASEE-gas specification 2005-001-02, should have a low impact on gas composition and reservoir geochemistry when the reservoir contains efficient pH-buffers such as calcite.

* Corresponding author.

E-mail address: irina.sin@minesparis.psl.eu (I. Sin).

1. Introduction

The energy transition from fossil sources to renewable but fluctuating energy sources faces a major challenge: how to develop storage capacity to improve supply stability. Among the various technologies, underground energy storage has a great potential in terms of both storage and power capacity, e.g. natural gas and hydrogen storage coupled with a power-to-gas system, compressed-air energy storage (CAES), and pumped hydro storage (Matos et al., 2019). Depleted gas fields, salt caverns and aquifers represent the three main geological storage options. Historically, France has essentially relied on aquifer storage, in gas volume percentage terms; since 1953 this has been mainly used for natural gas storage (Gombert and Ghoreychi, 2018). With the share increase of renewable energies in the energy mix these geological reservoirs are thus of a great interest (Juez-Larré et al., 2019; Mouli-Castillo et al., 2021). Nowadays, the underground storage of compressed air, hydrogen and biomethane stands out from the other renewable energy gas-based systems. However, the experience in storage of these new gas mixtures is limited compared to the rich history of the natural gas industry. Gas injection, or more precisely the injection of dioxygen gas $O_2(g)$, into a deep aquifer reservoir might induce a chain of complex biogeochemical reactions with a potential impact on groundwater resources, and also cause severe technical issues such as metallic corrosion in wellbores or rock-formation damages (Bui et al., 1990; Muschalle and Amro, 2013; Wang and Bauer, 2019; Guo et al., 2021).

Studies on CAES (Wang and Bauer, 2019) and carbon dioxide capture storage CCS (Jung et al., 2013; Pearce et al., 2016) with a range of 2 to 20 % of O_2 , respectively, showed that the injection of $O_2(g)$ into an anoxic geological porous formation containing pyrite can lead to pyrite oxidation producing high sulfate concentrations, acidic pH and a potential remobilization of metals and metalloids (e.g., As). This phenomenon is also well known in acid mine drainage (Evangelou and Zhang, 1995). Numerical codes applied to predict the $O_2(g)$ impact showed that the reaction of carbonate and plagioclase minerals could limit the acidification of the solutions (Wang et al., 2019; Ilojesi and Beckingham, 2021a; Pearce et al., 2022). Fe-(hydr)oxides precipitation has been observed in response to the release of Fe in the water phase and the oxidizing conditions (Pearce et al., 2016), which could induce pyrite passivation (Berta et al., 2016; Wang and Bauer, 2019). However, the magnitude of the described processes is controlled by gas-water-rock interactions that in turn strongly depend on the temperature, pressure, mineralogy and reactivity of the minerals. The various pyrite oxidation rates, or more precisely the various reactive surfaces used in modeling studies, are particular examples of the site-dependency of the same chemical process. Understanding the underlying geochemical process and their site-dependency is therefore essential to control the risks and impacts of $O_2(g)$ reactivity on the storage facility.

Reactive multiphase flow modeling can be used as a powerful tool to calculate and evaluate the spatial and long-term impact of gas storage scenarios in large porous media formations. Two modeling strategies have recently been used. The first strategy is site-independent. Inexpensive in terms of data measurement, this strategy is based on the so-called representative reservoir that can be used to test the influence of model parameters in gas storage scenario simulations (Bauer et al., 2012; André et al., 2014; Berta et al., 2017; Dethlefsen et al., 2017). However, the results of storage scenarios obtained from this method suffer from large uncertainties due to the significant influence of the parametrization (Dethlefsen et al., 2017). To limit these uncertainties, the second strategy site-dependent modeling needs large amounts of data from real sites to constrain and adjust the parametrization of storage in deep aquifer or depleted gas reservoirs. To the best of our knowledge, such field data which are representative of storage operations are rare in the literature. Regarding $O_2(g)$ reactivity in CAES in deep aquifers, the flagship site is the Pittsfield pilot where 6 MNm³ of dry air was injected into the St. Peter sandstones (USA) (Bui et al., 1990; Welch et al., 1990; Guo et al., 2021). Regarding $O_2(g)$ reactivity in CO_2 storage in deep aquifers, Wei et al. (2015) have studied and modeled field data on the geochemical impact of the injection of 200 tonnes of CO_2 and 30 tonnes of air into a sandstone aquifer in the pilot-scale experiment at Tongliao

(China). Todaka and Xu (2017) modeled geochemical field data from injection tests of $CO_2(g)$ with dissolved impurities (including O_2 up 7400 ppmv) in a siliciclastic reservoir at the Otway site (Australia).

The first objective of our study has been to present a set of field data that had been acquired on a pilot test of air as a cushion-gas injection into a deep sandstone aquifer in an underground natural gas storage facility located in Paris Basin, France, hereafter called the UGS reservoir. The cushion gas (also named base gas) is the minimal amount of permanently-stored gas that is necessary to keep a sufficient pressure in the storage facility to allow for injection and withdrawal operations. The air was injected at the edge of the storage aquifer for a period of three years, from 1989 to 1992. The air was partially depleted in $O_2(g)$ by adsorption on activated charcoal. But the remaining $O_2(g)$ content (8.1 %) made the cushion gas not as totally inert as a pure nitrogen gas $N_2(g)$ would have been. The operational objective was to substitute the initial cushion gas of natural gas with an alternative of no commercial value. The water chemistry and gas fraction composition were monitored before and after air injection for a period of 10 years.

The second and main objective of our study has been to develop a multiphase reactive transport model using the HYTEC code (van der Lee et al., 2003; Sin et al., 2017) to simulate the chain of chemical and hydrodynamic processes following the injection of $O_2(g)$ into the UGS reservoir. Despite earlier-mentioned numerical studies, none of them provides a full multiphase reactive transport model with advection of multiple reactive gases and their thermodynamic description. Few multiphase reactive transport codes exist (Steeffel et al., 2014; Sin et al., 2017) and, to the best of our knowledge, this is the first fully coupled multiphase reactive transport model based on field data. Mechanical processes are not considered. The model is parametrized on detailed characterization of the geological formation and the changes in the groundwater chemistry and gas composition. The full complexity of the reservoir was progressively implemented, starting with 0D-batch models focusing on geochemical kinetics, followed by 1D-radial and 2D-reservoir models to better capture the strong coupling between the chemical and multiphase transport processes including the structural trapping of gases. The consequences of the air cushion-gas on natural gas storage operations are discussed as well as implications for CAES, CCS and biomethane storage.

2. Gas storage site and field data

2.1. Geological and operational settings

The geological structure of the site is an anticlinal dome, approximately round, located in the Paris Basin, France (Fig. 1). The deep storage aquifer is a sandstone of Sequanian age (Upper Jurassic). The caprock and floor of the aquifer consist of a clayey marl and a microcrystalline limestone, respectively. The top of the aquifer reservoir stands at a depth of -470 m (-360 m above sea level) with a mean thickness of 25 m.

The storage facility has been in operation since 1965 and a pilot test of injecting air as a cushion gas took place from June 1989 to June 1992 (i.e. a duration of 3 years). Fig. 1 shows the inner zone of the gas storage facility containing about 30 natural gas wells (-360 m below sea level), while on the periphery there are several wells for environmental monitoring (from -400 to -450 m below sea level). The gas storage capacity is more than one billion of Nm³. The mean temperature and pressure in the aquifer reservoir during operations were 30 °C and 45 bars, respectively. The total mass of the injected air was about 0.15 billion of Nm³.

2.2. Natural and air cushion gas

Three monitoring wells were used to inject the air cushion-gas. They stood on the periphery of the storage aquifer and are denoted as Wells A, B and C hereafter (Fig. 1).

The mean composition of the injected natural gas in the years before 1989 was CH_4 (90 % in mol), other alkanes (6 %), N_2 (3 %), and CO_2 (0.7 %). The $O_2(g)$ content was below 0.01 %. The composition of the

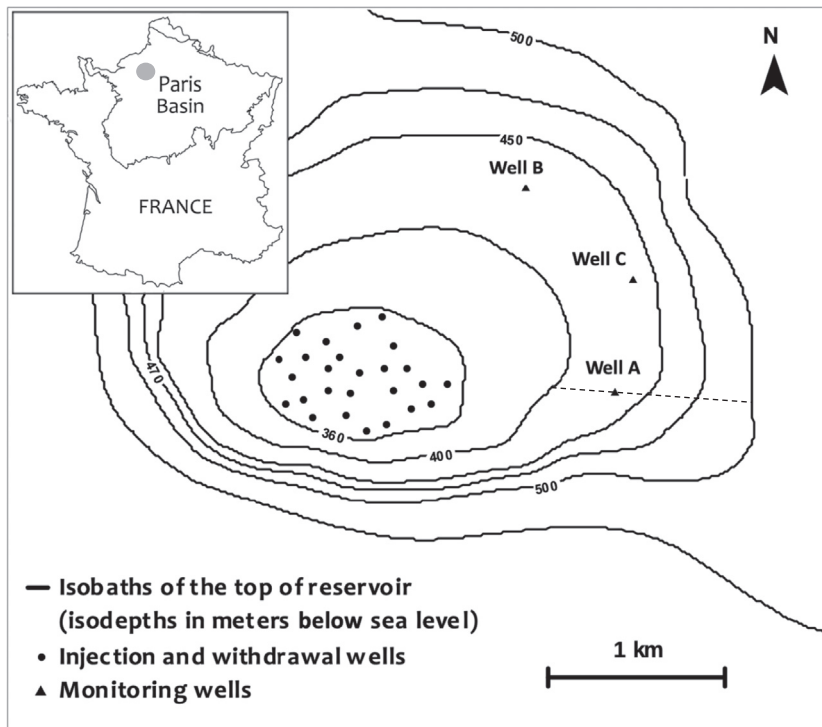


Fig. 1. Diagram of the UGS reservoir located in the Paris Basin with an inner top zone for natural gas wells (−360 m vs. sea level) and peripheral zones (about −425 m vs. sea level), with some of the monitoring wells that had been used for injecting the air cushion gas. The direction of the reservoir cross-section model presented in Section 4.3 is shown as dashed line.

injected natural gas changed very little from one year to the next. The mean composition of the air cushion-gas during the years 1989–1992 was N₂ (90.7 %), O₂ (8.1 %) and other gases (1.2 %) (see Table 1). CO₂(g) was only present at trace level, below 0.1 %.

The gas samples collected in Wells A and B were fully depleted in O₂(g) 6 to 9 months after the injection had been stopped (Fig. 2). The CO₂(g) mole fraction was initially under the detection limit and then increased to 1.2–1.5 % in Well B and 3.0–4.0 % in Well A after 6 to 8 months. The CO₂(g) contents were clearly above the 0.7 % of the natural gas. The CO₂(g) mole fraction kept slightly increasing up to the end of the sampling period to reach 2 % in Well B and 6 % in Well A. The composition in Well C was not determined during the first months; but after 8 months the CO₂(g) content had increased to 5 %, again significantly above the natural gas content. The percentages of N₂(g) and CH₄(g) are unfortunately not accurately known. Qualitatively, N₂(g) remained largely dominant in the gas phase.

2.3. Mineralogy of the reservoir

After crushing the reservoir rock samples to an 80-micron grain size, the mineralogy of the sandstone reservoir was quantitatively determined by X-ray diffraction (SIEMENS diffractometer) as well as Fourier-transform infrared spectroscopy (Perkin Elmer 16 PC spectrometer). The reservoir rock was mainly a sandstone cemented with calcite and clays. On average, the mineralogy was largely dominated by quartz with 65 % of the total mass of the rock, but also contained significant

Table 1 Measured and modeled compositions of the air cushion gas.

Gas (mol%)	Well A	Well B	Model
N ₂ (g)	90.7	90.5	90.7
O ₂ (g)	8.1	8.3	8.1
Ar(g)	1.2	1.2	1.2
CO ₂ (g)	Traces	Traces	0

amounts of calcite (20 wt%) and clayey phases (illite at 10 wt%, kaolinite at 5 wt%). Feldspars (probably potassic ones), pyrite and organic matter were present at a content of approximately 1 wt% each (see Table 2). Dolomite was only found at trace level. Mud logging and neutron-porosity logs were performed on several wellbores. The analyses showed that the relative content of calcite varied vertically and laterally in the sandstone formation. In particular, the vertical logging of the sandstone columns indicated that calcite was much less common in Well B compared to Wells A and C. The decrease in calcite was correlated to an increase in quartz.

2.4. Initial groundwater chemistry

The groundwater had been regularly collected at Well A (Fig. 3) and Well B (Fig. 4), both before and after the air injection period.

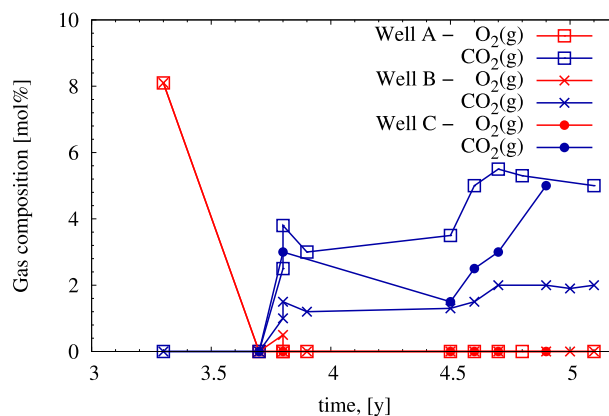


Fig. 2. Gas composition sampled in wellbores A, B and C over time. The air cushion gas was injected from year 0 to year 3.

Table 2
Measured and modeled mineralogies of the reservoir rock.

Mineral (wt%)	Measured	Model
<i>Carbonates</i>		
Calcite	20	20
Dolomite	Traces	0
<i>Aluminosilicates</i>		
Quartz	63	63
K-feldspar	1	1
Illite	10	10
Kaolinite	4	4
<i>Others</i>		
Pyrite	1–2	2
Organic matter	1–0	0

The water was sampled by borehole overflow and filtered at 45 μm for analyses. Despite some slight variations in the composition, the Schoeller diagrams indicate a homogeneous chemistry of the initial groundwater over time, in both wells. Na^+ was the main cation, whereas HCO_3^- and Cl^- were the main anions. The pH was around 7.5. The salinity was moderate, about 2.5–3 g/L. Not shown, the measured redox potentials, around -250 mV/SHE (standard hydrogen electrode), were in line with reducing conditions typical of underground waters. Furthermore, the dissolved SiO_2 concentration was initially at 0.25 mmol/L.

Table 3 reports the saturation indices of some key minerals with respect to the collected waters in Wells A and B. The saturation index SI of a given mineral is defined as:

$$SI = \log \left(\frac{IAP}{K_s} \right), \quad (1)$$

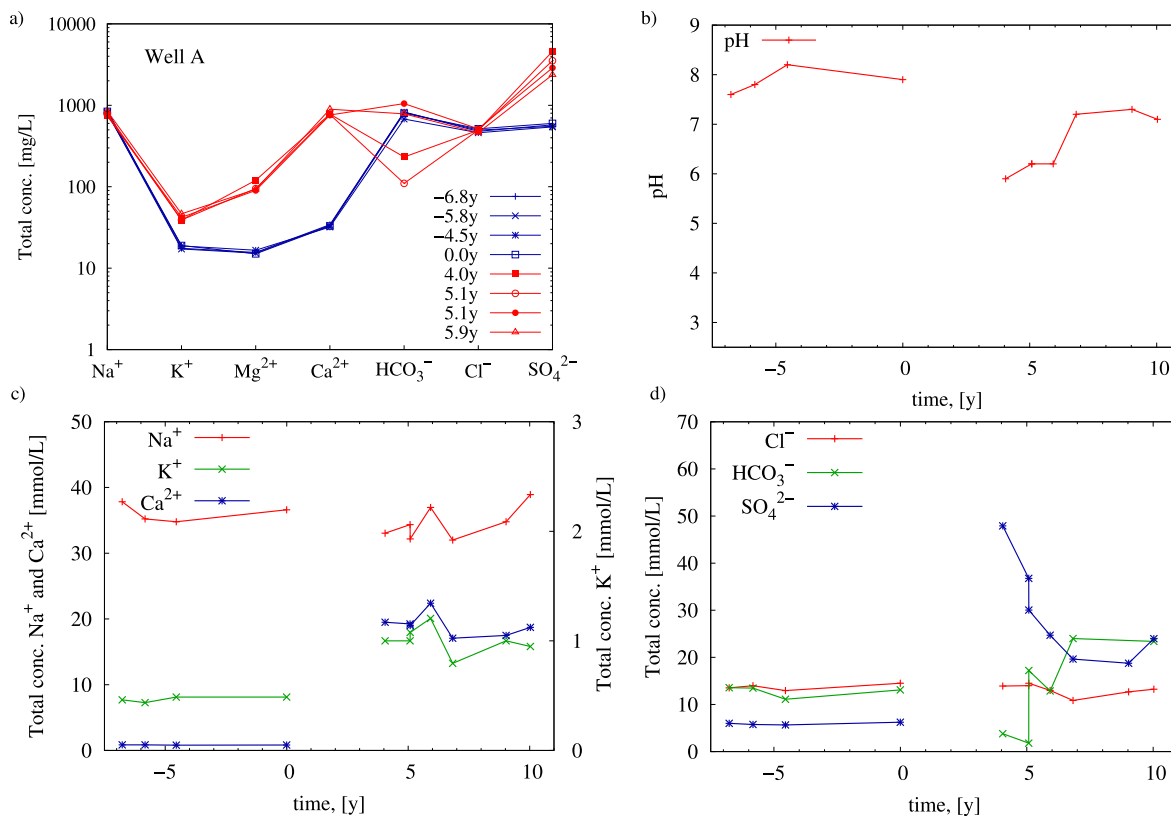


Fig. 3. Chemical composition of the reservoir water sampled in Well A. The air cushion-gas was injected from year 0 to year 3. a) Schoeller diagram and b) pH of groundwater, c) total concentration of cations Na^+ , Ca^{2+} and K^+ , d) total concentration of anions Cl^- , HCO_3^- and SO_4^{2-} before and after the air cushion-gas injection.

where IAP is the ion activity product and K_s is the solubility product constant at thermodynamic equilibrium. The mineral is close to equilibrium state with the groundwater when its SI is within the range $-0.5/ +0.5$, and may precipitate when SI is positive (supersaturation state), or may dissolve if present in the rock when SI is negative (undersaturation state). The SI values in Table 3 were calculated using the HYTEC geochemical module and the LLNL thermodynamic database (Wolery and Sutton, 2013). A temperature of 20 °C was assumed as the fluids partly cooled down while rising in the wellbore. The initial groundwaters were close to equilibrium with calcite and disordered dolomite (a proxy for magnesian calcite). Quartz was slightly supersaturated (i.e. not far from equilibrium), probably due to the cooling of fluids. Gypsum was clearly not present in the reservoir rock.

2.5. Groundwater chemistry after air injection

After the injection of the air gas cushion had been stopped, the pH was about 6 at Well A and as low as 3 at Well B. It is worth noting that the pH values had been confirmed by three different measurements made at intervals of a few days, with an average of 6.1 and 3.3 for Wells A and B, respectively. The pH was also measured in Well C after stopping the air injection, at around 6. The redox potential in Well A was around +350 mV/SHE at pH 6.2, that is to say mildly oxidizing. Concurrently to the decrease of pH, the analysis also showed a significant increase of the total concentrations of dissolved SO_4^{2-} , K^+ , Mg^{2+} and Ca^{2+} ; whereas the total concentrations of HCO_3^- decreased. As discussed in Section 4.1, all those elements were related to water-rock interactions driven by the injection. The dissolved total concentrations of Na^+ and Cl^- remained unchanged. Those two elements were not linked to any water-rock interactions and behaved like non-reactive tracers. Globally, the salinity of the affected waters increased up to 6 g/L, mainly due to the increase of Ca^{2+} and SO_4^{2-} concentrations. The dissolved SiO_2 concentration increased to 1 mmol/L in both wells after the air-cushion injection.

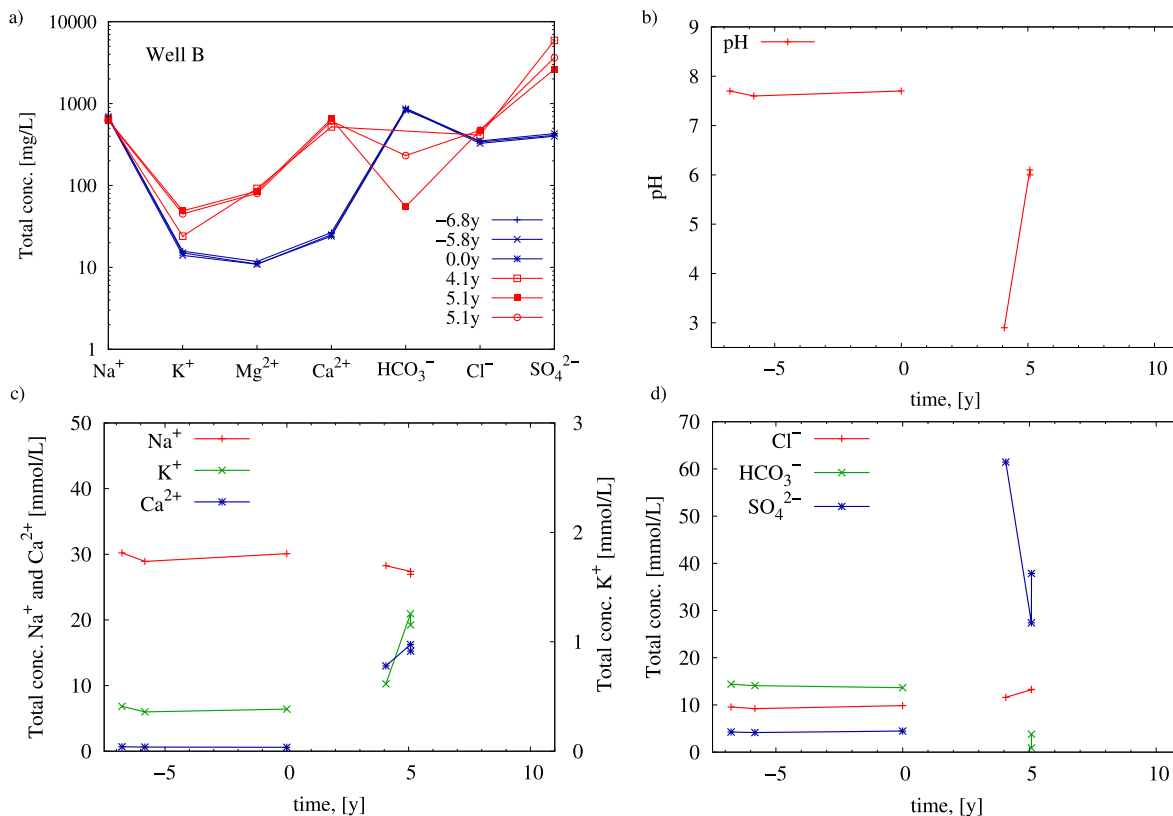


Fig. 4. Chemical composition of the reservoir water sampled in Well B. The air cushion-gas was injected from year 0 to year 3. a) Schoeller diagram and b) pH of groundwater, c) total concentration of cations Na^+ , Ca^{2+} and K^+ , d) total concentration of anions Cl^- , HCO_3^- and SO_4^{2-} before and after the air cushion-gas injection.

Over the longer term, the changes in chemistry were monitored for 6 years in Well A. The pH remained around pH 6 for two years and then came back to a neutral value very close to the initial state before the injection of the air gas-cushion. The SO_4^{2-} total concentration peak decreased by a factor of 3 within 4 years and stayed slightly above the initial-state concentrations. The HCO_3^- total concentrations progressively reverted back to their initial values. The K^+ and Ca^{2+} total concentrations remained slightly above the initial background levels in the long term. In respect of Well B, the chemistry was only analyzed for 2 years. During this period, the acidic pH quickly rose from the acidic value of 3.0 to a circumneutral value of 6.5, whereas the SO_4^{2-} total concentration decreased by a factor of 2. The other elements followed the same trend as in Well A, more concentrated in K^+ , Mg^{2+} and Ca^{2+} , but in general, not far from the initial groundwater chemistry.

Table 3

Saturation indices of some key minerals with respect to the collected waters calculated at 20 °C.

Time (years)	Calcite	Dolomite disordered	Gypsum	Quartz	Chalcedony
Well A					
-6.8	0.2	-0.2	-1.6	0.8	0.5
0.0	0.5	0.4	-1.6	0.8	0.5
4.0	-1.5	-4.2	0.2	0.8	0.5
5.0	-1.3	-3.8	0.1	0.6	0.3
5.1	-0.3	-1.8	0.1	0.4	0.1
5.9	-0.3	-1.8	0.1	0.6	0.3
6.8	1.1	1.1	-0.1	-	-
10.0	0.9	0.6	0.0	0.1	-0.2
Well B					
-6.8	0.2	-0.1	-1.8	0.8	0.5
0.0	0.1	-0.3	-1.6	0.7	0.4
4.0	-	-	0.1	1.3	1.0
5.1	-1.4	-4.0	0.1	0.6	0.3

The SI values of Table 3 indicate that the carbonate minerals (calcite, Mg-calcite) were found to be undersaturated immediately after the injection had stopped. This indicates dissolution in Well A and even a full depletion in Well B. In Well A, calcite again became close to equilibrium after a few months. Calcite and Mg-dolomite showed a supersaturation state in the longer term: this is not easily explained. The sampling methodology may have been changed with some artifact of partial $\text{CO}_2(\text{g})$ exsolution during the return of the water samples to the surface. Gypsum had undoubtedly formed (precipitated) during the air injection and the groundwaters remained in equilibrium with gypsum even at the longer duration of 10 years. Ultimately, there was no significant effect of the injection on the quartz minerals.

3. Multiphase reactive equations and parameters

The collected site data given in Section 2 were indicative of coupled physical and chemical processes in a porous medium. The interpretation of these data requires a multiphase reactive transport model, which is quite challenging because the gas-water-rock interactions change with regard to the injected gas and fluid displacement, becoming more complex and sophisticated since the transport is impacted by the chemistry as well. This section describes the reactive transport simulator, the principal governing equations and the parameters used for this study.

3.1. The HYTEC reactive transport simulator

The HYTEC reactive transport simulator (van der Lee et al., 2003) is a versatile general-purpose platform for the modeling of non-isothermal hydrodynamic and biogeochemical processes in saturated, unsaturated and multiphase porous and fractured systems. HYTEC has been successfully demonstrated in various benchmark studies (Carrayrou et al., 2010) and various applications, e.g. cement degradation (Seigneur et al., 2020), in situ recovery (Lagneau et al., 2019; Collet et al., 2022), geological storage

of radioactive waste (De Windt et al., 2014; De Windt and Spycher, 2019) and acid gases (Sin and Corvisier, 2019).

The multiphase reactive transport coupling in HYTEC is managed using an operator-splitting approach that solves governing equations of flow, transport and chemistry in a sequential iterative manner. This leads to a natural separation of operators by physics and makes the structure flexible and robust since each module can be easily verified. We present below a brief description of the flow, transport and geochemical governing equations used for the modeling (details can be found in Sin et al. (2017)).

3.2. Multiphase flow and transport

In multiphase flow, the mass conservation system for the gas and liquid phases is expressed as:

$$\frac{\partial(\rho_\alpha \phi S_\alpha)}{\partial t} = \nabla \cdot \left(\frac{\rho_\alpha k_{r\alpha}}{\mu_\alpha} \mathbb{K}(\nabla p_\alpha - \rho_\alpha \mathbf{g}) \right) + R_\alpha + q_\alpha, \quad (2)$$

where ρ_α , S_α , $k_{r\alpha}$, μ_α and p_α are the mass density, saturation, relative permeability, viscosity and pressure, respectively, of fluid phase α ($\alpha = l$ for liquid, or g for gas). ϕ is the porosity, \mathbb{K} the intrinsic permeability tensor, and \mathbf{g} the gravitational acceleration vector. R_α is the reaction term, and q_α the external source/sink term of fluid phase α .

Based on primary species formalism (Lichtner, 1996; van der Lee, 2009), the gas and liquid transport equation is:

$$\frac{\partial \phi S_\alpha c_{\alpha,i}}{\partial t} = \nabla \cdot (D_\alpha^e \nabla c_{\alpha,i} - c_{\alpha,i} u_\alpha) + R_{\alpha,i}(c_{\alpha,i}, c_{s,i}) + q_{\alpha,i}, \quad (3)$$

where $c_{l,i}$ is the total mobile liquid concentration of primary species i and $c_{g,i}$ the gas concentration of species i . The diffusion-dispersion operator D_α^e also includes the tortuosity effects represented by the Millington-Quirk model:

$$D_\alpha^e = \phi^{n_b} S_\alpha^{n_s} D_\alpha, \quad (4)$$

where n_b and n_s are fitting parameters and D_α the molecular diffusion coefficient. Dispersion effects were ignored, although the numerical dispersion arising from the discretization method is $\Delta x/2$, which gives a maximum dispersivity of 1 m in the 1D-radial model and the same value in the 2D model near the injection well. The advective fluxes are given by the multiphase flow Eq. (2): $u_\alpha = -\frac{k_{r\alpha}}{\mu_\alpha} \mathbb{K}(\nabla p_\alpha - \rho_\alpha \mathbf{g})$. The reaction term $R_{\alpha,i}$ depends on the mobile $c_{\alpha,i}$ and immobile $c_{s,i}$ concentrations of species i .

The relative permeability models were as follows:

$$k_{rg} = k_{rg \max} \left(\frac{S_g - S_{gr}}{1 - S_{gr} - S_{lr}} \right)^{n_{kr_g}}, \quad k_{rl} = \frac{S_l - S_{lr}}{1 - S_{gr} - S_{lr}}, \quad (5)$$

where the fitting parameters $k_{rg \max}$ and n_{kr_g} are the maximum value and the power parameter, 0.9 and 3 in this study, respectively. S_{lr} and S_{gr} are the residual liquid and gas saturations, respectively. The gas and liquid pressures in Eq. (2) were related by capillary pressure. The model of Brooks and Corey (1964) was employed with the prescribed maximum value of 1 GPa (for other parameters see Table 4). The relative permeability and capillary pressure models were set using history matching at the reservoir scale.

The reservoir parameters are listed in Table 4. The gas density was calculated by the PR78 model of Robinson and Peng (1978), whose accuracy has already been demonstrated for air and CO₂ mixtures (Sin, 2015; Nazeri et al., 2017; Sin and Corvisier, 2019). The solution changed with gas-water-rock interactions and also depended on the system pressure and temperature. The liquid density was then managed by the model of McCain Jr. (1991) that gives a good description of fluid density depending on the total dissolved solids under the pressure and temperature conditions in the reservoir. The initial density was 996 kg/m³. The average water viscosity at the reservoir temperature and pressure was taken as the liquid

Table 4

Reservoir parameters and fluid properties, see text for details.

Reservoir parameters	
Temperature	30 °C
Porosity ϕ	0.2
Permeability \mathbb{K}	$1 \times 10^{-12} \text{ m}^2$
Residual gas and liquid saturation S_{ar}	0.1, 0.15
Capillary pressure	Brooks and Corey (1964)
entry pressure	1 kPa
power	2
Gas and liquid relative permeabilities	Eq. (5)
Fluid properties	
Gas composition: N ₂ (g), O ₂ (g), Ar(g), CO ₂ (g), H ₂ O(g)	
Gas and liquid diffusion D_α	$2 \times 10^{-5}, 1 \times 10^{-9} \text{ m}^2/\text{s}$
Millington-Quirk	Eq. (4)
porosity power n_b	1.3
gas and liquid saturation power n_s	3.3 and 1
Gas density ρ_g	Robinson and Peng (1978)
Liquid density ρ_l	McCain Jr. (1991)
Gas and liquid viscosity μ_α	$1.88 \times 10^{-5}, 7.97 \times 10^{-4} \text{ Pa}\cdot\text{s}$

viscosity, and the average air viscosity for the gas phase using the estimation of National Institute of Standards and Technology (NIST, Lemmon et al. (2013)).

3.3. Gas-liquid equilibrium

The phase equilibrium handled by the fugacity-activity ($\varphi - \gamma$) approach is as follows:

$$f_i^g = P y_i \varphi_i^g = K_i^H \gamma_i c_i = f_i^l, \quad (6)$$

where y_i is the mole fraction of species i in the gas phase, and φ_i^g the fugacity coefficient. The latter is derived from the Peng-Robinson equation of state PR78 (Robinson and Peng, 1978) that considers the repulsive and attractive forces using the critical pressure, temperature and acentric factor of component. It allows us to calculate the fugacity coefficient of component in a mixture employing the combining and mixing rules with corresponding binary interaction parameters for each pair of components. Table S1 presents the binary interaction parameters used in this work. The temperature-dependent Henry's constant $K_i^H = K_i^H(T, P)$ includes the Poynting factor which corrects the fugacity with respect to the pressure (Michelsen and Mollerup, 2007), this is especially important at reservoir conditions. The apparent molar volume of solutes was calculated using the Helgeson-Kirkham-Flowers equation. The vapor H₂O(g) was considered in the system. Although the pore space was initially saturated, a small amount of water evaporated when the air was injected. The Henry constants of the LLNL database (Wolery and Sutton, 2013) used in this study are given at 30 °C in Table S2. The temperature was assumed to be constant throughout this study. γ_i is the asymmetric activity coefficient of species i , and c_i is the molal concentration of species i in the liquid phase. For example, O₂(aq) for O₂(g), see Table S2. Depending on the reaction, the term $\gamma_i c_i$ becomes the activity of the dissolved species with respect to the mass action law.

The asymmetric approach Eq. (6) is universal: it combines the equations of state and activity models that allows to accurately model the thermodynamic properties of gas mixtures. For example, solubility of CO₂, O₂, CH₄, H₂, SO₂, N₂, Ar, H₂S in water, brine and aqueous solutions (Corvisier et al., 2013; Hajiw et al., 2018; Sin and Corvisier, 2019; Chabab et al., 2020a, 2020b).

3.4. Geochemical thermodynamic equilibrium

Assuming that the aqueous species are at thermodynamic equilibrium, HYTEC solves the chemical system for independent primary species and derives the secondary concentrations from the linearly dependent reactions

(van der Lee et al., 2003). The mass balance then stems from the equilibrium reactions and mass action law and it is assembled as the total concentration for each primary species, that is actually a mathematical sum to conserve during the simulation.

The LLNL thermodynamic database (Wolery and Sutton, 2013) was used. Table S3 gives the formation constants of the mineral considered in this study. The activity of the dissolved species and water was calculated by the B-dot and Helgeson formalisms (Helgeson, 1969). In total, the geochemical model contained about 100 aqueous species, 5 gas species, and 8 solids.

3.5. Kinetics of mineral dissolution and precipitation

Both thermodynamic equilibrium and kinetic control are considered in HYTEC for the dissolution and precipitation of minerals. For kinetically controlled reactions, the following rate law based on transition state theory (Lasaga, 1984) was used for the carbonates and silicates:

$$r_{kin} = \frac{d[M]}{dt} = A_v (k_{acid} a_{H^+}^{n_{H^+}} + k_{neur}) \left(\left(\frac{IAP}{K_s} \right) - 1 \right) \quad (7)$$

where $[M]$ is the mineral concentration, A_v is the volumetric surface area of the mineral M (related to the specific surface area A_s by the relation by $A_v = A_s \times [M]$), k is the kinetic dissolution/precipitation rate constant, a_{H^+} is the proton activity and n_{H^+} is a fitting parameter. The terms IAP and K_s are the same as in Eq. (1) and stand for the thermodynamic-dependent term. The rate law covered the initial near-neutral pH conditions as well as the possible shift towards the acidic range due to pyrite oxidation.

Table 5 gives the parameters of Eq. (7) for the different minerals of the reservoir rock. The kinetic parameters of calcite, K-feldspar and quartz came from the well-known compilation of Palandri and Kharaka (2004). Plummer et al., 1978 experimentally showed that the rate of calcite dissolution decreased by two orders of magnitude when the partial pressure in $CO_2(g)$ increased from 0 to 1 bar. The impact is more important at higher pH (Plummer et al. (1978); Sjöberg and Rickard (1984); Brantley et al. (2008)). Accordingly, the original neutral rate constant from Palandri and Kharaka (2004) was reduced to 1×10^{-07} , i.e. a factor of 18. The kinetics of calcite dissolution remained nevertheless considerably higher compared to the aluminosilicates. The original k_{neur} and k_{acid} constants for K-feldspar were divided by 10 to better fit the field K^+ concentrations (alternatively, the specific surface A_s could have been reduced by a factor 10), as discussed in Section 4.1. There was no catalyzing effect of acidic pH on quartz dissolution. The dissolution rate constants and the pH-dependent reaction orders for illite and kaolinite were obtained from Huertas et al. (1999), Köhler et al. (2003) and Marty et al. (2015). As discussed by Köhler et al. (2003), the apparent dissolution rate of kaolinite is slightly superior to that of illite. The mineral reactive surface areas are given in Table 5. The surface areas of K-feldspar and quartz were estimated assuming an average grain size of 400 – 200 μm as determined by granulometric analysis performed on materials collected in Well A. The surface areas of kaolinite and illite were set to a much higher value due to the micron-size of clayey minerals.

Table 5

Kinetic rate parameters of minerals used in the study (Eqs. (7) and (9)), which are identical for dissolution and precipitation.

Mineral	k_{neur} (mol/m ² /s)	k_{acid} (mol/m ² /s)	n_{H^+}	n_{O_2}	A_s (m ² /g)	f
Calcite	1×10^{-07}	1×10^0	1.1	–	1×10^{-2}	–
Quartz	5×10^{-14}	–	–	–	1×10^{-2}	–
K-feldspar	1×10^{-14}	8×10^{-12}	0.5	–	1×10^{-2}	–
Illite	1×10^{-15}	2×10^{-12}	0.6	–	2×10^1	–
Kaolinite	1×10^{-14}	8×10^{-12}	0.5	–	2×10^1	–
Pyrite	5×10^{-09}	–	–0.11	0.58	1×10^{-1}	1.0 (base case) 0.1 (field factor case)

The oxidation of pyrite is complete due to the high O_2 gas content. That is to say that sulfide, S(-I), initially present in $FeS_2(s)$ is oxidized into SO_4^{2-} , S(VI), and ferrous iron, Fe(II), is oxidized into ferric iron, Fe(III). The Fe(III) aqueous concentration drastically increases, generating the formation of amorphous and crystallized Fe(III)-solid phases. Goethite is most likely to precipitate at pH values ranging between 3 and 8 (Pearce et al., 2016; Wang and Bauer, 2019). As a consequence, the model simulates the following general chemical reactions:



The kinetic rate law of pyrite oxidation used in this study is derived from the well-known relationship by Williamson and Rimstidt (1994) and Rimstidt and Vaughan (2003):

$$r_{kin,pyrite} = \frac{d[FeS_2]}{dt} = -f A_v k a_{H^+}^{n_{H^+}} a_{O_2(aq)}^{n_{O_2}}, \quad (9)$$

where the field factor f takes into account the reduced reactivity of the surface area of pyrite in natural environments. This type of factor has been previously discussed in Swoboda-Colberg and Drever (1993); White and Brantley (2003) Klein et al. (2013); Bourg et al. (2015); Wang and Bauer (2019). Eq. (9) is dependent on the dissolved $O_2(aq)$ activity and is valid from a neutral to acid pH range, with a slight inhibition of pyrite dissolution under acidic conditions. The kinetic parameters used for modeling pyrite oxidation are detailed in Table 5. Nicholson et al. (1988) investigated pyrite oxidation in a carbonate solution and demonstrated that the oxidation rate is largely controlled by the mineral's reactive surface area. The pyrite surface area of Table 5 corresponds to the lower range of values attributed to framboidal pyrite, whose morphology (as opposed to cubic pyrite grains) was observed in the present reservoir rock. Such a reactive surface could be affected by different processes, e.g. the precipitation of ferric oxide on the pyrite surface inducing kinetic rate decrease and low $O_2(aq)$ diffusion coefficient through this passivating layer (Nicholson et al., 1990). To account for the possible reduction of available pyrite surface sites, a field factor of 0.1 was applied to the reactive surface initially considered.

The precipitation of goethite is usually rapid compared to the other mineral reactions and can be modeled at local equilibrium (Marty et al., 2015). As a reasonable approximation, and for the sake of minimizing the modeling parameters, the kinetics of pyrite dissolution was assumed to be rate limiting for the kinetics of formation of the secondary minerals goethite and gypsum. Therefore, goethite was modeled at thermodynamic equilibrium. Gypsum precipitation was under a fast kinetic control (Eq. (7), rate constant k_{neur} of 10^{-8} mol/m²/s, the same volumetric surface area as calcite) for easing numerical convergence.

The set of kinetic laws and parameters selected for this study was able to simulate the chemical changes in the reservoir. This set is also generally in good agreement with the parameters of Marty et al. (2018) for the weathering of pyrite in argillaceous rock under atmospheric air, as well as the parameters of Wang and Bauer (2019) for the geochemical reaction induced by $O_2(g)$ by CAES in an underground reservoir. There are, however, some differences among all these modeling studies. It is indeed tricky to assign a single set of kinetic parameters to a complex and heterogeneous rock. Moreover, kinetic rates measured in the laboratory are commonly

found to be up to 3 orders of magnitude greater than those observed in the field (Swoboda-Colberg and Drever, 1993; White and Brantley, 2003; White, 2008; Klein et al., 2013; Bourg et al., 2015; Wang and Bauer, 2019). All these points will be further discussed in Section 5.

4. Modeling results

4.1. Batch modeling of the gas-water-rock interactions

A batch model is an essential first step to ascertaining the relevant reactions and the system's overall changes. In order to model and interpret the collected data from Section 2, we considered a nominal volume located in the reservoir while subjected to the injection of the depleted air Section 2.

4.1.1. Model setup

The initial chemistry of the aquifer water in the model corresponded to the measured field data before injection (Fig. 3). Only the total dissolved HCO_3^- concentration was modified to ensure equilibrium with calcite. The composition of the modeled air cushion-gas (Table 1) and mineralogy (Table 2) were very close to the site data. A single grid node of 1 m^3 was designed to investigate the changes in the zone near the wellbore, which was initially almost fully saturated by the injected air: porosity 0.2, initial gas saturation $S_g = 0.8$. The fugacity of the injected gases was maintained during the simulation to reproduce an air injection without gas flow. The model permitted a gas accumulation while pressure built up and compressed the system, conserving the total volume constant and preserving the gases inside the model. No entry flux was allowed, since we wanted

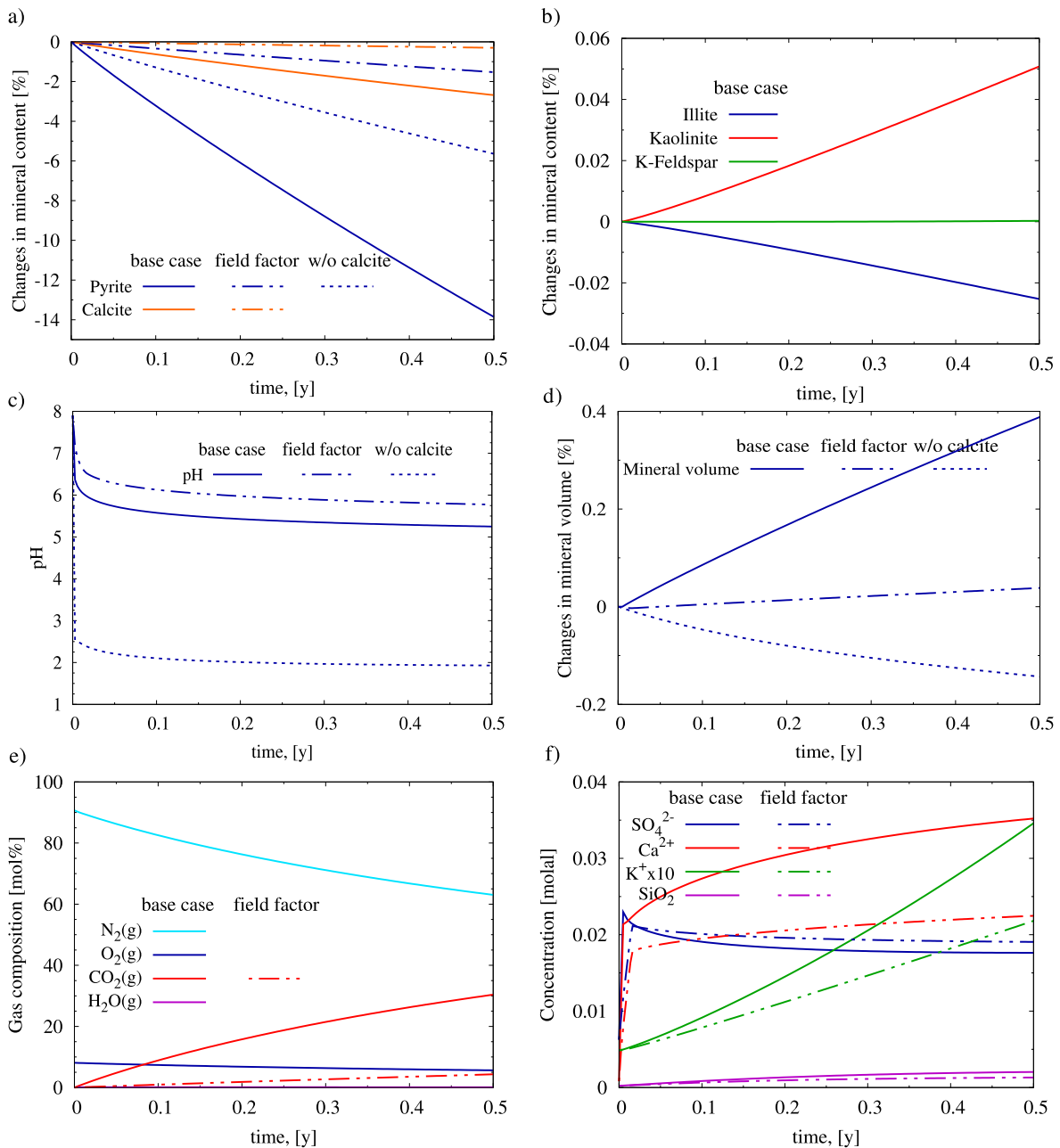


Fig. 5. Batch modeling of the local zone changes over time of the groundwater chemistry, mineralogy and gas composition inside the air plume over 0.5 years, for the Base case, Field factor case (field factor) and Base case without calcite (w/o calcite) inside the air plume. a) and b) Changes in mineral content in % with regard to the initial mass in kg; c) pH; d) changes in mineral volume in % with regard to the initial mineral volume; e) gas composition in mol%; f) total dissolved concentrations of SO_4^{2-} , Ca^{2+} , K^+ , and SiO_2 in molal, total dissolved K^+ concentration is multiplied by 10 for the sake of clarity.

to study the local geochemical changes without the effects of external factors. The average reservoir pressure was 45 bar and temperature was set constant at 30 °C. Since the model was “zero-dimensional”, the viscous effect was absent and the viscosities were then assumed constant for both phases.

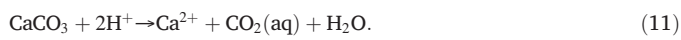
4.1.2. Modeling results

4.1.2.1. Groundwater chemistry and mineralogy changes. Fig. 5 shows the changes with time of the groundwater chemistry, mineralogy and gas composition inside the air plume over 0.5 years. Three scenarios were assessed: (i) the Base-case scenario with the full dataset described in Section 3, (ii) an extreme scenario without any calcite, to simulate the sandstone layers that are locally impoverished in calcite (especially around Well B) and (iii) a scenario considering a slower kinetic rate for pyrite using the Field factor case to simulate coating or ageing.

The geochemical driving force of the full system is the oxidation of pyrite by $O_2(aq)$ (Fig. 5a) sustained by $O_2(g)$ solubilisation in the liquid phase. Eq. (8) clearly indicates that 1 mol of oxidized pyrite and 1 mol of precipitated goethite produces 4 mol of protons, and therefore may significantly acidify the reservoir groundwater. Pyrite oxidation and acidification of the solution are supported by previous modeling studies of compressed air (Wang and Bauer, 2019) and CO_2 geological storage Vu et al. (2018). Indeed, the calculated pH decreases within the first days following the cushion-gas injection in the three scenarios, (Fig. 5c), but its magnitude is noticeably different. Carbonates as calcite can efficiently buffer the acidic plume according to the following reactions from circumneutral pH

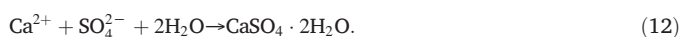


to acidic pH range



The calculated pH obtained with the Base-case mineralogical assemblage and kinetics is in good agreement with the pH values of about pH 6, monitored near Well A right after the air injection was stopped (Fig. 3). The calculated values are lower than the field data: pH 5.3–5.5 from 1 month to 0.5 years. The $CO_2(aq)$ exsolution, during the return of the samples to the surface at atmospheric pressure for pH measurements, might explain the discrepancy between the measured and real in situ pH values. Another explanation might be that pyrite oxidation proceeds at a lower rate, as calculated in the Field factor case in which the calculated pH ranges between 5.8 and 6.0. Eventually, pH becomes as low as 2 after 0.5 years in the scenario without calcite. It is worth noting that it is similar to the field acidic data measured in Well B, i.e. pH 3. The groundwater collected in this borehole resulted from the mixing of water from different sedimentary horizons of the sandstone which are more or less rich in calcite, which probably explained why the pH is not as acidic as the extreme case calculated without any calcite buffering. It is worth noting that clayey and silicate minerals forming the reservoir's rock also have some pH buffering ability (albeit much less efficient than calcite) that limits the pH decrease around 2 in the simulation.

The combination of Eqs. (8), (10) and (11) leads to the increase of Ca^{2+} and SO_4^{2-} concentrations that finally results in the saturation with gypsum:



Pearce et al. (2016) confirmed gypsum precipitation following the injection of a gas mixture containing 2 % of $O_2(g)$ in a sandstone aquifer, using scanning electron microscopy. The calculated total Ca^{2+} and SO_4^{2-} concentrations are regulated by the mutual near-equilibrium state of calcite and gypsum. Gypsum formation occurs early in the simulations (Fig. S1a), which explains the plateau reached in both concentrations in Fig. 5f. The calculated total concentrations ($[Ca^{2+}]_T = 25 - 35 \text{ mmol/L}$; $[SO_4^{2-}]_T = 20 \text{ mmol/L}$) are fairly close to the field data ($[Ca^{2+}]_T =$

$15 - 20 \text{ mol/L}$; $[SO_4^{2-}]_T = 40 - 50 \text{ mmol/L}$) obtained right after the air injection was stopped. The calculated content in SO_4^{2-} is well above the background field data, i.e. 5 mmol/L, but lower than the measured data at the end of the air injection test. Gypsum precipitation is probably not fully at thermodynamic equilibrium, which is in agreement with the weak supersaturation state (SI of 0.1–0.2) of Table 3. The calculated total Ca^{2+} concentrations (20 mmol/L) match the field data better, while decreasing the rate of pyrite oxidation (Field factor case). The calculated total SO_4^{2-} concentration soon becomes unrealistically high in the absence of calcite (Fig. S1b), since it is no longer possible to precipitate gypsum without any sources of Ca^{2+} .

In the Base case, the mass changes in illite, kaolinite, K-feldspar and quartz are insignificant over 0.5 years due to their slow kinetics at neutral pH (Fig. 5b). While illite slowly dissolves, kaolinite forms, providing protons. The illite dissolution results in a weak increase of total K^+ concentration over time, from the background concentration of 0.1 mmol to 1 mmol/L (mean field data) or 2 mmol/L (mean calculated data) after air injection. The transformation of illite (possibly K-feldspar) to kaolinite under weak acidity is a well-documented process in the superficial weathering of rocks. The total concentration of dissolved silica is almost constant. However, the very acidic pH calculated in the scenario without calcite strongly enhances the kinetic of dissolution of illite and K-feldspar that is catalyzed by protons (Eq. (7) and Table 5). Illite dissolution is the main source of dissolved K^+ . The released potassium should allow for jarosite precipitation with available SO_4^{2-} and Fe^{3+} that would limit this increase. Since jarosite is not considered in the scenario without calcite, the K^+ concentration is overestimated.

4.1.2.2. Changes in gas composition. Both the gas volume and pressure of the system change during pyrite oxidation and calcite dissolution (Fig. 5e). Since gases cannot escape from the closed batch system, they accumulate over the simulation duration. The amount of $N_2(g)$, $O_2(g)$, and $Ar(g)$ remains fixed, while the mole fractions change due to $CO_2(g)$ production. Indeed, the calculated $CO_2(aq)$ concentration increases due to calcite dissolution, which in turn increases the $CO_2(g)$ content in the gas phase by exsolution, according to the Henry's law.

The magnitude of $CO_2(g)$ production is sensitive to the considered scenarios. For the Base-case scenario, the released $CO_2(g)$ reaches 30 mol% after 0.5 years, whereas the mole fractions of the other gases decrease. The calculated value largely overestimates the 2 to 6 mol% monitored in situ at all 3 wellbores. Conversely, the attenuation of pyrite kinetics by the field factor reduces the amount of dissolved calcite and thus the mole fraction of $CO_2(g)$ to 4 mol% after 0.5 years. In the Base-case scenario, the pressure builds up but the gas saturation grows only from 0.8 to 0.84 because of the increased density. Although the gas density is low at the beginning, 52 kg/m³, the growing CO_2 content in the gas phase increased it up to 80 kg/m³ after 0.5 years of injection.

4.1.2.3. Changes in porosity. In the Base case, 14 % of the initial pyrite mass is consumed after 0.5 years of constant $O_2(g)$ supply, compared with only 6 % in the scenario without calcite, since acidic conditions limit the dissolution of pyrite (Fig. 5a). However, overall, mineral dissolution and precipitation only result in a small decrease of the aquifer porosity, by approximately 1.6 % and 0.2 % of the initial value for the Base case and Field factor case, respectively. In the presence of calcite, the dissolution of pyrite and the precipitation of goethite are almost equal in volume terms. Interestingly, the mass of gypsum is almost twice as much as the dissolved calcite. Furthermore, the molar volume of gypsum (74.7 cm³/mol) is much higher than the molar volume of calcite (36.9 cm³/mol), so this yields a slight swelling. These processes were also observed during a compressed air energy storage facility in a deep aquifer (Succar et al., 2008; Ilojesi and Beckingham, 2021b). The mineral volume increases up to 0.4 % and 0.04 % in the Base and Field factor cases, respectively (Table 6, Fig. 5d). The changes in porosity are then insignificant, and the pressure build-up is mainly due to the exsolution of $CO_2(g)$.

Table 6

Calculated changes in the batch model at 0.5 years. Gases in mol%, pressure P in bar, minerals in % with regard to the initial mass, mineral volume V_{min} in % with regard to the initial volume.

Scenario	pH	CO ₂	O ₂	N ₂	P	Pyrite	Calcite	Illite	Kaolinite	K-feldspar	V_{min}
Initial state	7.9	–	8.1	90.7	45	–	–	–	–	–	–
Base case	5.3	30.4	5.6	63.0	56	–14.0	–2.7	–0.03	0.05	3×10^{-4}	0.4
Field factor case	5.8	4.3	7.7	86.7	46	–1.5	–0.3	–0.02	0.03	2×10^{-4}	0.04

4.2. One-dimensional radial injection model

4.2.1. Model setup

A one-dimensional (1D) radial flow model was used to study the coupled geochemical and transport processes during the injection of air with 8.1 % O₂ into the saturated infinite reservoir. The two scenarios,

Base case and Field factor case, were still maintained. Approximately 144 MNm³ of air was injected through Well A during 1099 days starting in 1989. The injection rate q_{air} in the model Eq. (2) was scaled for a 10 m long wellbore. The formation pressure was set at 45 bar. The air composition was similar to that used in the batch model, as well as mineralogy, see Tables 1 and 2. The reservoir characteristics corresponded to site

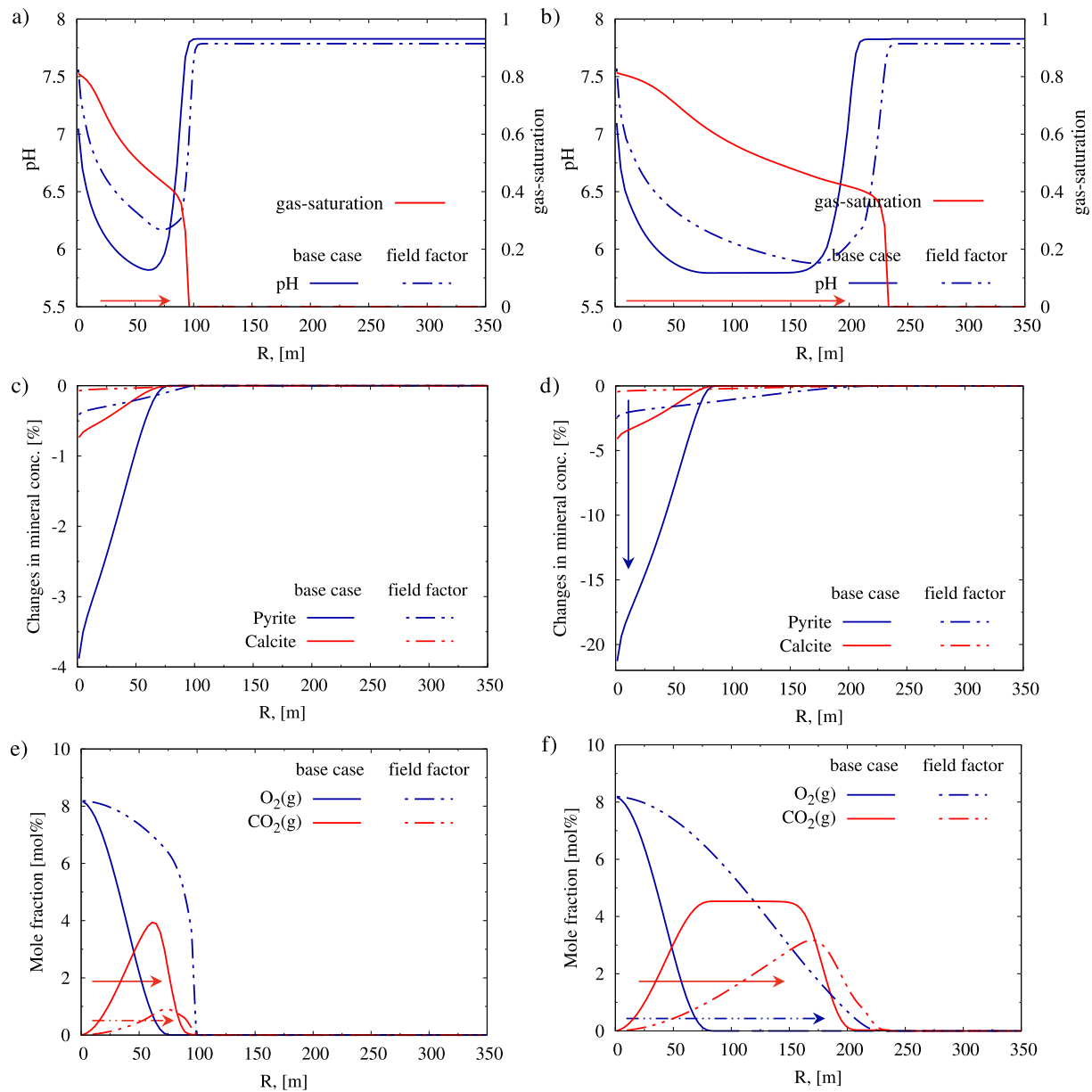


Fig. 6. 1D-radial modeling of the groundwater chemistry, mineralogy and gas composition after 30 days (left) and 0.5 years (right) of air injection for the Base case (solid line) and Field factor case (field factor, dashed line). Profiles are plotted as a function of radius from the injection well, R. a) and b) gas saturation and pH; c) and d) changes in mineral content in % with regard to the initial mass in kg; e) and f) mole fraction of gas species O₂ and CO₂ in mol%.

measurements, and the empirical parameters were calibrated using the site data, they are listed in Table 4. In contrast with the batch model, the injection model added consideration of diffusion and advection.

4.2.2. Modeling results

Fig. 6 illustrates the changes in mineralogy, reservoir groundwater and gases after 30 days and 0.5 years of air injection in both scenarios. The gas injection builds up the pressure near the wellbore creating the pressure gradient that evacuates the fluid in the direction of Darcy velocity. The profile of gas saturation is typical (Fig. 6a–b). The acidification of the reservoir groundwater (Fig. 6a–b), following the oxidation of pyrite, is buffered by calcite (Fig. 6c–d), as in the batch model. However, pyrite dissolution occurs only near the wellbore during all the injection period in the Base case (solid lines in Fig. 6). Approximately 22 % of the pyrite disappears by 0.5 years creating the impact radius of 75 m around the injection point. A similar tendency can be observed for calcite: even though the gas plume extends to nearly 250 m, the minerals are intact beyond 75 m radius. The profile of $O_2(g)$ is static (steady-state) during the simulation due to the rapid consumption by pyrite (Fig. 6e–f). It is worth noting that the distribution of $O_2(g)$ is strongly correlated to pH. We will develop the pH behavior near the injection point further in this section. Interestingly, firstly $CO_2(g)$ is exsolved after calcite dissolution in the near-well zone, and then it is pushed away by gas flow to the front of the plume where it accumulates. This can be seen in both scenarios, especially in the Base case with higher pyrite kinetics where calcite dissolves in the first ~80 m. However, $CO_2(g)$ migrates beyond 80 m, filling the pore space in front (Fig. 6e–f). The pore volume slightly decreases in the impact zone due to the precipitation of goethite and gypsum (Fig. S2).

In the Field factor case (dashed lines in Fig. 6), pyrite dissolution drops from 22 % to 2.4 % in the near-wellbore zone, which is consistent with the order of magnitude of $f = 0.1$. However this time the dissolution of pyrite and calcite gradually advances with the injected gas. Oxygen spreading develops along with other injected gases, contrary to the Base case with $f = 1$. There is less dissolved pyrite as expected, and hence the environment is less acidic, less calcite is dissolved, so less $CO_2(g)$ is exsolved. At the beginning of the injection, only a small amount of CO_2 is produced, approximately 1 % versus 4 % in the Base case at 30 days (Fig. 6e–f). Then, the maximum CO_2 content rises up to 3.2 % at 0.5 years versus 4.5 % in the Base case, suggesting that the acidification of the reservoir groundwater is continuing.

4.2.3. Analysis of multiphase Damköhler number for oxygen

The modeling results of the radial transport models reveal a great impact of the kinetic rate on the acidity changes, gas species and also on the extent of the affected zone. To better understand the controlling nature of kinetic rates, we employed a dimensionless advective Damköhler number Da_l that represented the dominance of advection relative to the chemical reaction in the system. The traditional definition of Da_l can be expressed as follows (Steeffel, 2008):

$$Da_l = \frac{\tau_{adv}}{\tau_r} = \frac{\frac{L}{u}}{\frac{L}{A_v k}} \quad (13)$$

where τ_{adv} is the characteristic time for advection to transport a species c , e.g. $SiO_2(aq)$, with velocity u through the characteristic length and τ_r is the characteristic time for reaction of c consumption $r_{kin} = A_v k((c/K_s) - 1)$, e.g. $SiO_2(s)$ precipitation, similar to Eq. (7). However, this definition is irrelevant in our study because the pyrite requires oxygen to be dissolved and its kinetic rate depends on the concentration of O_2 , which is initially absent in the system and supplied only by the injected air. Consequently, the driving force but also the controlling factor is oxygen and not the solubility constant of the mineral K_s as established in the traditional Da_l , Eq. (13). Despite this, a Damköhler number can be adapted for oxygen $O_2(g)$ consumption in a multiphase system.

Combining the transport equations in gaseous and liquid phases Eq. (3), the reactive transport equation of oxygen can be written in the classic form Accumulation = Flux + Reaction:

$$\frac{\partial}{\partial t} (\phi S_g c_{O_2(g)} + \phi S_l c_{O_2(aq)}) = \nabla \cdot (D_g^e \nabla c_{O_2(g)} + D_l^e \nabla c_{O_2(g)}) - \nabla \cdot (c_{O_2(g)} u_g + c_{O_2(aq)} u_l) + R_{O_2, pyrite} + q_{O_2(g)}, \quad (14)$$

Oxygen is very slightly soluble, i.e. $\log K^H = 2.9$, and the solubility of gases is instantaneous, so the contribution of dissolved oxygen in the advection-reaction competition is negligible. More specifically, the accumulation term of dissolved oxygen $\phi S_l c_{O_2(aq)}$ can be estimated. The gas-liquid equilibrium Eq. (6) yields $c_{O_2(aq)} = f_l^0 / (K_l^H \gamma_l)$, where f_l^0 is between 0 and around 3.7 bar that corresponds to 8 mol% in the injected gas at reservoir conditions, the fugacity coefficient γ_l being around 1.023. The system is partially saturated, $S_l < 1$. The accumulation term of $O_2(aq)$ then lies in the range between 0 and 10^{-4} contrary to the accumulation term of $O_2(g)$ reaching $\sim 10^{-1}$. Since the system is driven by gas injection $q_{O_2(g)} > 0$, the system is advection-dominant, and diffusion can be ignored. The velocity of the liquid phase is non-zero but still slower than that of the gases since the medium is unsaturated. The advection term of dissolved oxygen $c_{O_2(aq)} u_l$ is smaller by 3–4 orders of magnitude than $c_{O_2(g)} u_g$. Then, the reactive term $R_{O_2, pyrite}$ represents the consumption by pyrite:



This simply yields that 1 mol of dissolved pyrite consumes 3.75 mol of oxygen with the kinetic rate $r_{kin, pyrite}$, which itself depends on oxygen, Eq. (9). Again, since the dissolution of oxygen in the solution is instantaneous and the solubility of $O_2(g)$ is low, then oxygen consumed by pyrite is actually gaseous oxygen, resulting in $R_{O_2, pyrite} = R_{O_2(g), pyrite} = -\phi S_g 3.75 r_{kin, pyrite}$. To resume, Eq. (14) states that Accumulation of oxygen increases with Flux, i.e. the advective term $c_{O_2(g)} u_g$, and decreases with Reaction, which is the dissolution of pyrite in our system.

Considering the local meaning of Da_l , the following expression for oxygen consumption in multiphase porous media can then be adapted:

$$Da_{l, O_2} = \frac{\tau_{adv}}{\tau_r} = \frac{\frac{blackL}{u_g}}{\frac{c_{O_2(g)}}{R_{O_2(g), pyrite}}} = \frac{\frac{[L]}{[LT^{-1}]}}{\frac{[NM^{-1}]}{[NM^{-1} T^{-1}]}} = [-] \quad (16)$$

$$= \frac{R_{O_2(g), pyrite}}{c_{O_2(g)} u_g} = \frac{\phi S_g 3.75 r_{kin, pyrite}}{c_{O_2(g)} u_g},$$

where $[L]$, $[T]$, $[M]$, and $[NM^{-1}]$ are units of length, time, mass and concentration respectively. This definition of Da_{l, O_2} is derived from the mass balance of oxygen in reactive transport and it is still in agreement with to the traditional Da_l , with $\tau_{adv} = L/u_g$ being the characteristic time for the advective transport of $O_2(g)$, and $\tau_r = c_{O_2(g)} / R_{O_2(g), pyrite}$ being the characteristic time for the pyrite dissolution under kinetic control. The characteristic length L is equal to 1 m. By construction, the derived Damköhler number Eq. (16) means that the dominant advection regime $Da_{l, O_2} \ll 1$ occurs for a high injection or low kinetic rate. The term u_g is the Darcy gas velocity and not the pore gas velocity. The dominant reaction regime $Da_{l, O_2} \gg 1$ indicates that the dissolution of pyrite is faster than oxygen supply with the velocity u_g over $L = 1$ m in our unsaturated porous media. Finally, for the equilibrium state $Da_{l, O_2} = 1$, the transported material is consumed, and the advective τ_{adv} and reactive τ_r times are equal. Fig. 7 gives the changes with space and time of the calculated Da_{l, O_2} numbers for both the Base and Field factor cases.

Both scenarios have very low Da_{l, O_2} near the injection well during the entire simulation time (red lines in Fig. 7) indicating an advection-dominant regime, when there is more injected $O_2(g)$ than can be consumed by pyrite. This is also in agreement with the basic – neutral pH near the injection point followed by a transition to the acidic conditions (Fig. 6),

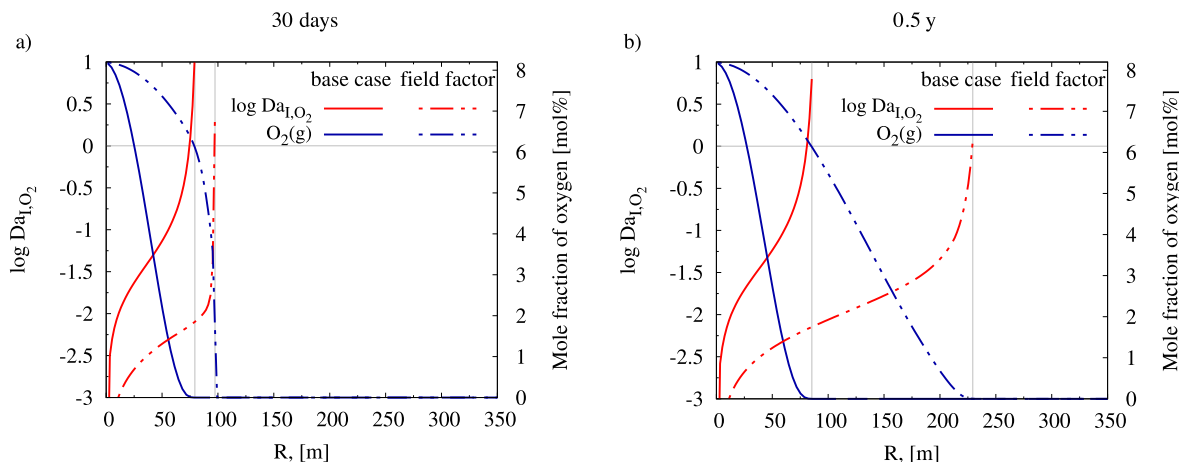


Fig. 7. Advective Damköhler number Da_{I,O_2} in [-] (red lines) and mole fraction of $O_2(g)$ in mol% (blue lines) after 30 days (a) and 0.5 years (b) of air injection in Base and Field factor cases (solid and dashed lines, respectively), see details in the text. (For interpretation of the references to color in this figure legend, the reader is referred to the web version of this article.)

that corresponds to the decreasing gas velocity $\sim 1/R$ further from the well, so the Damköhler number rapidly climbs up.

In the Base case, the reactive and advective times are equal, i.e. $Da_{I,O_2} = 1$ at 75 m by 30 days and at 81 m by 0.5 years (red solid lines in Fig. 7). The rapid rise of Da_{I,O_2} means that even though the kinetic rate decreases downstream of the flow, the gas velocity decelerates even faster, resulting in the disappearance of oxygen. The transition state $Da_{I,O_2} \sim 1$ (i.e. $\log Da_{I,O_2} \sim 0$) of the system corresponds to the $O_2(g)$ slope as expected (blue solid lines in Fig. 7). The shape and area of the Da_{I,O_2} curve are almost unchanged. Beyond this radius of rapid kinetics, the pH is buffered, and the flat path for $CO_2(g)$ can be observed in Fig. 6. This model predicts a rapid dissolution of pyrite and calcite in the affected zone near the injection point, suggesting the complete exhaustion of pyrite and calcite dissolution by 20 % after 2–3 years, followed by progressive pyrite depletion zone by zone, which would not be consistent with the observations in the field.

Interestingly, the Field factor case gradually expands the zone of reaction dominance from 97 to 229 m at 30 d and 0.5 years, respectively (red dashed lines in Fig. 7) promoting the dissolution in the whole area of the injected gas. After 30 days of injection, the advection is dominant at a radius of 100 m around the injection point. The steep rise Da_{I,O_2} at 100 m correlates with the sharp drop of O_2 (Fig. 7). Nevertheless the transition zone keeps steadily developing with the time since the velocity decreases faster than the reactive rate does, resulting in an almost linear O_2 slope. This enables liberating protons for calcite dissolution in the whole extent of the injected gas (Fig. 6). This last scenario was chosen for the reservoir scale modeling.

4.3. Reservoir scale model

4.3.1. Model setup

The natural gas is injected and withdrawn each year through the top point of the dome-like aquifer extending down underneath the impervious caprock. Injecting the cushion gas on the periphery of the gas reservoir maintained the pressure in the reservoir during intensive gas withdrawal. The injected air was then constrained both by the in situ gas and the anticlinal structure of the aquifer. A two-dimensional (2D) reservoir cross-section model aimed to place the studied reactive transport system into more realistic conditions, with gravity effects reproducing the observations in the field (Section 2). The direction of the 2D model is shown as dashed line in Fig. 1. The regular mesh was rotated to reproduce the tilt of the aquifer and it is refined in the stored gas zone and near the injection well, whereas large cells were employed in the far field (Fig. 8a).

The presence of CO_2 in the methane mixture (0.7 mol%) was ignored in order to investigate the production of CO_2 coming from calcite dissolution without any ambiguity. The in situ natural gas was then

represented by $CH_4(g)$ only. Moreover, the advection was eliminated in this methane-rich gas region, yet the elements could diffuse. The aquifer was initially fully saturated with a hydrostatic pressure distribution. The hydrodynamic and geochemical parameters were identical to those used for the 1D-radial reactive transport model (Field factor case).

4.3.2. Modeling results

Fig. 8 gives the modeling results after 0.5 years of the injection of the air cushion-gas. Air is heavier than the in situ methane-rich gas but lighter than the formation water. At reservoir pressure and temperature conditions, the density of the air-rich mixture is approximately 59 kg/m^3 and the density of the methane-rich gas is 32 kg/m^3 . The air therefore remains below the gas reservoir because of gravity and, additionally, it is constrained by the geological structure retaining the build-up of air under the aquifer sealing and methane-rich zone (Fig. S3a). Less soluble nitrogen $N_2(g)$ (Fig. S3b) and argon $Ar(g)$ (not shown) are homogeneously distributed in the air plume with a slow gradient beneath the zone of the in situ methane which diffuses in the gas phase. The spread of O_2 (Fig. 8b) is in good agreement with the results of the 1D-radial model: oxygen is concentrated near the wellbore and gradually disappears at the periphery of the air plume due to the growing dominance of the kinetic rate over the transport rate. The transition state can be seen on the Da_{I,O_2} map (Fig. S3c). Calcite dissolution (Fig. S3d) is faster near the injection point than on the periphery of the air plume, as seen with the previous models. Once CO_2 is exsolved, it is then displaced by gas flow and accumulates downstream of the gas current (Fig. 8c). The $CO_2(g)$ reaches 2.4 mol% by 0.5 years of injection which is in agreement with the order of magnitude of $CO_2(g)$ found by the 1D and batch models. As mentioned above, $CO_2(g)$ is initially absent in the model; the observed diffusion of $CO_2(g)$ in the natural gas zone arises from calcite dissolution, this amount is negligible. Changes in pH and Eh (Figs. 8d and S3e) are in agreement with the results of the previous models. The aquifer acidification reaches pH 5.8. Gas distribution and mineral changes (Figs. 8 and S3) are in good agreement with the 1D-radial model as well.

The Damköhler number (Fig. S3c) is in the range of the previously calculated results of Section 4.2.3, which gives us the confidence that the 1D-radial and 2D reservoir scale models are consistent. Yet, Da_{I,O_2} is slightly higher compared with the 1D-radial model. This comes from a lower velocity profile in the reservoir model. By construction, the injection rate in the vertical cross-section geometry is lower than that of the radial model and additionally, the gas velocity is limited by the in situ methane zone and the aquifer base. Consequently, this yields a slightly slower pyrite rate, however the decrease is smaller than that of the velocity, resulting in a higher Da_{I,O_2} , faster $O_2(g)$ consumption. The $O_2(g)$ plume radius of the 2D model is around 170 m versus 229 m in the 1D-radial model.

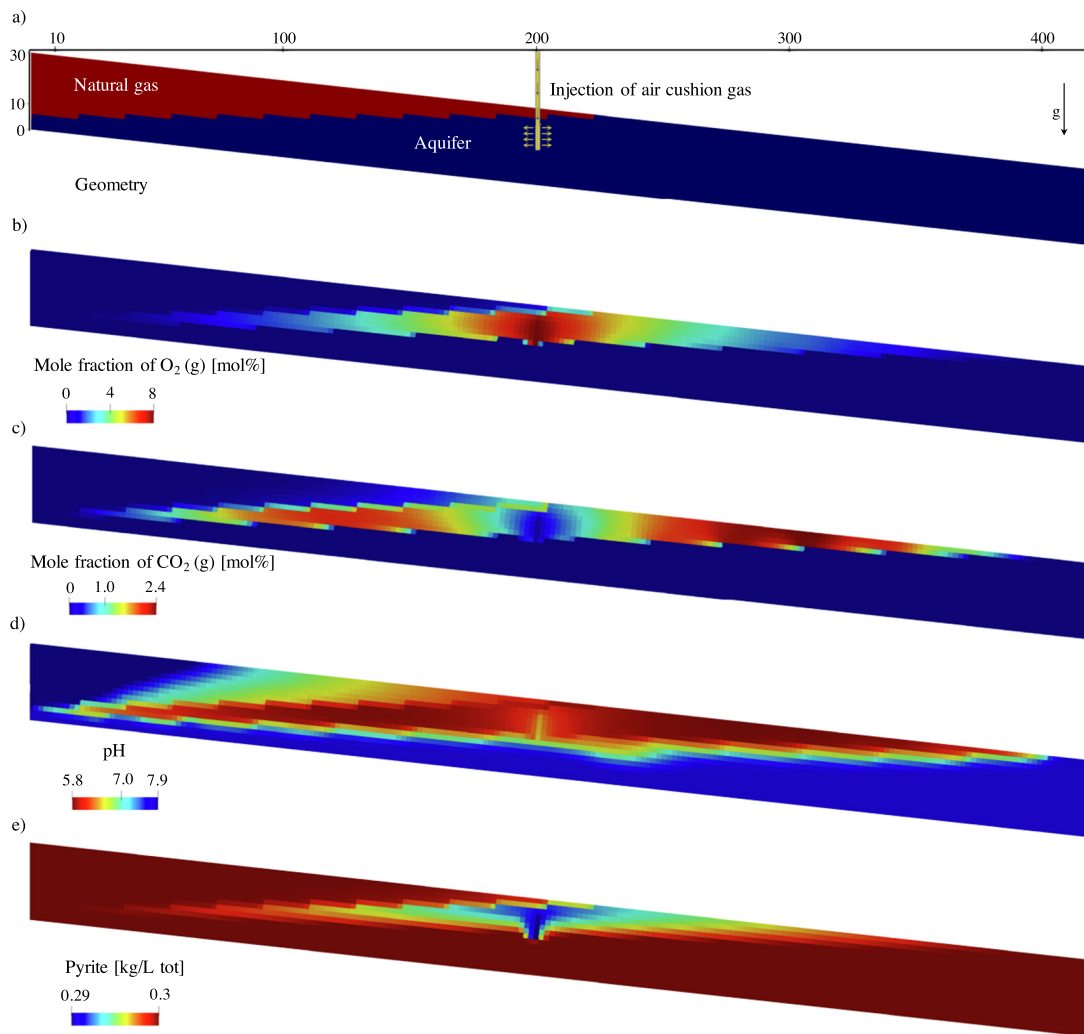


Fig. 8. 2D-reservoir scale modeling of the groundwater chemistry, mineralogy and gas composition after 0.5 years of air injection in tilted aquifer for the Field factor case. Cross section view. a) Geometry: in situ natural gas (red), aquifer (blue), and injection well (yellow); the presented gridblocks are $2\text{ m} \times 2\text{ m}$; the full geometry of the aquifer is 1 km long and 30 m high with variable gridblock size. b) and c) mole fraction of gas species O_2 and CO_2 in mol%. d) pH; e) pyrite concentration in kg divided by the initial total porous volume, i.e. normalized to the initial porosity, kg/L tot. (For interpretation of the references to color in this figure legend, the reader is referred to the web version of this article.)

A 2D-radial configuration on the basis of the 1D-radial model in Section 4.2 was also studied. The gas was injected in the upper part of the grid similarly to the wellbore configuration depicted in Figs. 8a but without the aquifer tilt and in situ gas. In these modeling results (not shown), the buoyant plume of injected air forms a bubble, migrates upwards and then continues to spread laterally below the low-permeable seal (caprock) similarly to the injection of CO_2 in saline aquifers (Sin and Corvisier, 2019). Since the air is light even at moderate-to-high pressure and temperature, by continuing the air injection, the buoyant plume then becomes a thin disc of a larger diameter. Consequently, there is a low content of $\text{O}_2(\text{g})$ and, hence of $\text{CO}_2(\text{g})$, circa $\sim 0.2\%$ at 0.5 years. This yields low kinetic rates of pyrite versus advection even in the radial geometry. Interestingly, $\text{CO}_2(\text{g})$ also accumulates around the wellbore in the base of the air plume. At the beginning of injection, the concentration of O_2 is high enough at the injection point to promote pyrite oxidation, and the produced CO_2 accumulates around the wellbore. The plume becomes narrower afterwards letting CO_2 to be trapped in the residual gas saturation near the wellbore. So, the physics was actually correct but not representative of the observed processes in the field because of the missing so-called physical or structural trapping known from the carbon dioxide storage concept (Metz et al., 2005). More precisely, when injected on the periphery of the natural gas reservoir, the cushion gas builds up below physically bound

traps – the impermeable caprock and the reservoir itself. The modeling results given in Figs. 8 and S3 confirm this hypothesis.

5. Discussion

5.1. A unique set of field data

To the best of our knowledge, our study presents a unique set of field data acquired from June 1989 to June 1992 on a pilot test of air cushion-gas injection in a deep-aquifer natural gas storage facility in the Paris Basin. These data were obtained under conditions representative of an operational facility over a large spatial scale and a duration of 3 years. The initial state of the reservoir (mineralogy, petrographical log, groundwater chemistry, hydrodynamic parameters) before the air injection was fully characterized as well as the operational parameters (wellbore geometry, pressure, injection rate, cushion-gas composition). After the injection period, a consistent set of data on groundwater chemistry, as well as the analysis of the gas phase in CO_2 and O_2 were collected. A postmortem analysis of the rock disturbed by air injection and the CH_4 content in the collected gas was unavailable. But generally, the field data were sufficiently rich to develop a multiphase reactive transport model of the disturbance induced by the air injection. Our study does not investigate the return to the

natural background that was measured for more than 10 years. Modeling work along these lines is still under progress.

Previously, injection tests of an air cushion-gas in a deep aquifer reservoir (made of limestone and sandstone layers) were performed from August 1979 to August 1981 in the natural gas storage facility at Saint-Clair-sur-Epte (Paris Basin, France) with air containing 5 % of O_2 and 11 % of CO_2 (Laille et al., 1988). The gas sampling showed a complete loss of O_2 but no significant variations of the initially high CO_2 component. Unfortunately, details on the groundwater chemistry were not provided by the authors. A more complete case is the Pittsfield pilot of a compressed air energy storage (CAES) opened in 1982 in the St. Peter sandstone in the USA (Bui et al., 1990; Welch et al., 1990; Guo et al., 2021). About 6 million Nm^3 of dry air was injected to form a large gas bubble. For storage periods of several months, the $O_2(g)$ content was found to have completely disappeared from the reservoir, and CO_2 contents in the gas phase as high as 2.5 mol% were reported (Bui et al., 1990). A series of experimental tests were also carried out to reconstruct the history of the pilot data, pointing out the direct relation between pyrite and oxygen consumption, i.e. 3.75 mol of oxygen for 1 mol of dissolved pyrite (Eq. (15)). Everything in these field and lab findings suggested that the pyrite oxidation coupled to calcite dissolution was the major culprit, which is consistent with our study.

5.2. In situ reactive sequence of oxygen consumption

Fig. 9 presents the conceptual chain of physico-chemical reactions that takes place when oxygen is injected in a deep aquifer reservoir. This sequence has been based on the literature and assessed in our work by the adequate reactive transport modeling of the field data of air injection into sandstone reservoir in the Paris Basin (France). 1D-radial and 2D-reservoir scale modeling have provided modeling results in good agreement with the field data on the gaseous changes (CO_2 and O_2), as well as the water chemistry changes (pH, redox potential, concentrations in major cations and anions), due to air injection. Oxygen present in the cushion gas induces mineral alteration, i.e. oxidation of pyrite crystals, leading to the acidification of the formation water that promotes the dissolution of clays, feldspar, quartz and, more importantly, carbonates as calcite. The kinetics of the dissolution of carbonates are indeed more rapid by orders of magnitude compared to aluminosilicates. Due to calcite dissolution

and partial acidification, the reservoir groundwater leads to the degassing of $CO_2(g)$ and its gradual accumulation in the cushion-gas plume observed both in the field data and modeling results. Gypsum and goethite are secondary minerals that precipitate at a relatively rapid kinetic rate. They might have a feedback effect of reducing the pyrite and calcite kinetics by a passivation process as discussed below.

The present reactive transport models have not considered the heterogeneity of the reservoir rock mineralogy. More acidic conditions have been measured (pH 3) and modeled (pH 2) in Well B corresponding to sedimentary levels poor in calcite. Despite this limitation, the order of magnitude of $CO_2(g)$ produced in situ is in agreement with the observed data. The reservoir scale model provides 2.4 mol% of CO_2 by 0.5 years, whereas the field data presented in our study vary from 2 to 6 mol% after 4 years.

By using a fully coupled multiphase reactive transport modeling, we have not only investigated the evolving geochemistry induced by oxygen, but also the impact of the chemical reactions on the gas displacement. Former studies have performed similar batch and reactive transport models in the context of CAES, but used an immobile gas zone as a diffusive source of oxygen, preventing the gas from displacement (Berta et al., 2017; Wang and Bauer, 2019). Although multiphase flow and thermodynamics have been intensively studied in the context of the geological sequestration of carbon dioxide, the modeling of gas mixtures in reactive transport is still challenging. Indeed, the oxidation of pyrite has been observed by a series of CO_2 injection tests into the Paaratte formation (Otway Basin, Australia) using carbon dioxide with impurities, SO_2 , O_2 and NO_x . In Todaka and Xu (2017) and Vu et al. (2018), the injected gas impurities were modeled as dissolved due to missing equations of state. The authors showed that the impurities had a minimal impact on both the acidity of the formation water and the water geochemistry. Injecting oxygen, or gas species in general, as dissolved results in the transport of aqueous species with Darcy velocity of the liquid phase that is different from the velocity of the gas phase, which can be significantly higher due to the injection rate. In addition to variations in gas density and composition, the spreading of co-injected gases can then be hindered due to changing coupled reactive processes. To overcome these issues, group contribution equations of state are used to accurately describe the thermodynamics of gas mixtures, and the fugacity-activity approach allows us to correct solubility of gases as described in Section 3. This method has already been validated by

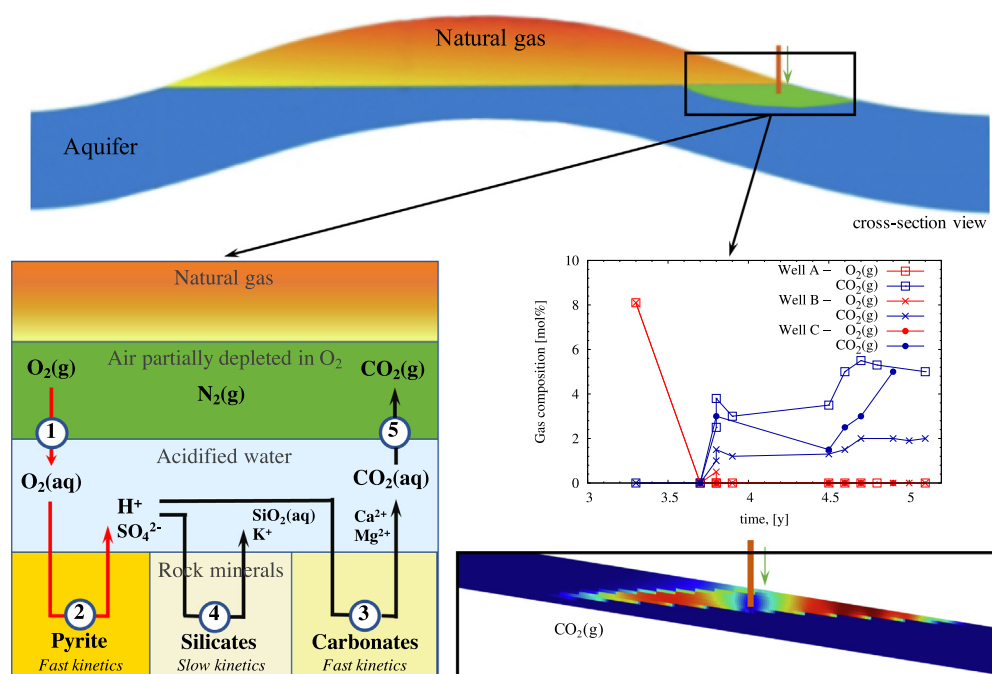


Fig. 9. Conceptual chain of geochemical reactions induced by air injection into a deep aquifer gas reservoir.

modeling experimental results in the context of impure carbon dioxide storage (Corvisier et al., 2013; Sin and Corvisier, 2019). However, there is a lack of data on oxygen binary parameters due to its high reactivity. Interactions of oxygen with argon and methane have therefore been assumed negligible in our study.

Microbial activity has been excluded from our study. Aerobic bacteria can consume oxygen with organic matter or reduced components, S^{-} , Fe^{2+} , as electron donors. Heterotrophic bacteria can also be a source of CO_2 . In this respect, recent experiments with bacteria have been performed with samples from a natural gas reservoir in the South Aquitaine sedimentary basin in France (Haddad et al., 2022). The authors showed that bacterial diversity and activity was significantly reduced with the injection of 1 % O_2 . The authors also observed an increase in dissolved sulfate concentration due to pyrite oxidation. Even though some bacteria strains survived in such oxic conditions, their activity was shown to be negligible. Regarding the present studied sandstone formation, the proportion of organic matter is rather low and isotopic analysis confirmed that the sampled $CO_2(g)$ originated from the chemical dissolution of carbonates and not from microbial fermentation or respiration (Schmitt et al., 1996). We give this information as indicative only, but Welch et al. (1990) have also pointed out that a 13-C isotope analysis suggested a non-bacterial origin for the $CO_2(g)$ produced into the St. Peter sandstone formation at the Pittsfield CAES pilot project.

5.3. Multiphase-transport versus pyrite-oxidation kinetics

Our modeling results have emphasized the importance of reactive transport when hydrodynamics and geochemical processes are strongly coupled and can be either transport- or reaction-limited. The transition from the batch model to the 1D-radial transport model has shown that scale-changing can be game-changing. In the Base (Field factor) case, the batch and radial transport models predict a maximum gas content in $CO_2(g)$ of 30 % (4.3 %) and 4.5 % (3.2 %) after 0.5 years. The differences lie not only in the quantity of produced $CO_2(g)$ but also in the distribution and spatial extent of the reactions. Introducing Da_{I,O_2} has allowed us to evaluate the predominant chemical reaction and advection regimes, and the transition between them. The calculation of Da_{I,O_2} numbers has also illustrated the importance of the kinetic rate of pyrite whose magnitude can shift the transition between transport- or reaction-limited regimes. Among other effects, a reduction in the overall reactive surface of pyrite would correspond to a lower Da_{I,O_2} allowing for a greater oxygen migration in the reservoir.

Table 7 compares several kinetic rate laws and parameters used for modeling pyrite oxidation by dissolved oxygen gas in geologic formations. The first four kinetics laws are variants of the well-known relationship of Williamson and Rimstidt (1994), but differ in the setting of the specific reactive surface that varies from $6 \times 10^{-4} m^2/g$ (Wang and Bauer, 2019) to $7 \times 10^{-2} m^2/g$ (Marty et al., 2018). For comparison, the reactive surface of pyrite calibrated in field models of geological carbon storage varies between 1×10^{-4} and $4 \times 10^{-2} m^2/g$ (Bourg et al., 2015). The specific surface adjusted to the Field factor case ($1 \times 10^{-2} m^2/g$) is within the range of these data, although towards the upper limit.

The lowest specific surface of Wang and Bauer (2019) has been considered in a batch model of a CAES system where pH reached 6 after 12.5 years and dropped to 1.5 after the full depletion of dolomite and calcite.

Table 7
Kinetic rate constants of pyrite oxidation by dissolved oxygen gas.

Reference	k [mol/m ² /s]	n_{H^+}	n_{O_2}	A_s [m ² /g]
Williamson and Rimstidt (1994)	$1 \times 10^{-8.2(\pm 0.1)}$	-0.11	0.5 (± 0.04)	
Wang and Bauer (2019)	$1 \times 10^{-8.2}$	-0.11	0.5	6×10^{-4}
Marty et al. (2018)	$1 \times 10^{-8.4}$	-0.18	0.5	7×10^{-2}
This work (Field factor)	$1 \times 10^{-8.3}$	-0.11	0.58	1×10^{-2}
Todaka and Xu (2017)	4×10^{-11}	-	-	8×10^{-3}

Compared to our field data and modeling results, the pH values with and without calcite are similar but the time scale is much longer. Still, the attenuation of the pyrite oxidation rate has been experimentally observed but at near-neutral and alkaline pH (Nicholson et al., 1990; Huminicki and Rimstidt, 2009; Pérez-López et al., 2009; Berta et al., 2016). According to these studies, Fe(III)-precipitates on pyrite grains grow in thickness and create a coating that reduces the diffusion of oxygen by several orders of magnitude. Berta et al. (2016) have proposed a kinetic rate based on Williamson and Rimstidt (1994) but taking into account the development of a passivation layer on the pyrite surfaces at near-neutral pH. The decrease of the pyrite kinetic rate by such a passivation process would probably become important in the long-term evolution of the present site.

5.4. Consequences for natural gas storage in deep aquifers

The modeling results have indicated that the exsolved $CO_2(g)$ is pushed away from the injection wellbore as long as air is being injected. However, when the injection of air is finished, the $O_2(g)$ should be completely disappeared (high Damköhler number) and CO_2 production should stop. Then the remaining $CO_2(g)$ could diffuse towards the near-wellbore zones. Additionally, the seasonal withdrawal of natural gas creates a significant fluid displacement that could bring CO_2 close to the monitoring wells, as observed in the gas sampling (Fig. 2). Similarly, while acidity production stops with air injection completion, some acidic water might migrate towards the near-wellbore zones. Corrosion of the well casing and tubing materials (steel components) might be exacerbated once in contact with acidic and CO_2 -enriched groundwaters (Schutt and Lyle, 1998; Martin, 2002; Grise and Saldanha, 2008). This possible detrimental effect on corrosion should be balanced by the fact that strongly acidic conditions only occur in the absence of carbonate minerals, and that field data have indicated that even these acidic waters were rather rapidly neutralized (e.g. in Well B, from pH 3 after the air injection stopped, to pH 6 0.5 years later). Still during the period of air injection, the modeling results have led to a lateral expansion of the $O_2(g)$ plume around the wellbores of several tens of meters. This steady-state concentration of O_2 would also probably worsen the corrosion of casings and tubing.

Furthermore, the present study looks at the processes at a reservoir scale (from a meter to a few hundreds of meters) and it does not bring any insights on what might occur around the wellbore at a smaller scale, where particles can be transported and deposited due to changing physical and chemical mechanisms, e.g. divergence and convergence of streamlines near the well, coating of grains with iron oxide and changes in the carbonates and clays with pH, giving rise to potential clogging issues.

Field data have shown that pH decreases due to pyrite oxidation but is buffered around 5.8–6 by carbonate minerals, calcite in particular, and conversely, that pH drops to an acidic level of around 3 when calcite is depleted or absent. This is supported by the present modeling results from batch to reservoir models. Steel et al. (2018) assessed the buffering effect of calcite by adding it to the brine at pH 2. The dissolution of calcite produces a weak acid HCO_3^- and stabilizes the pH at 5.7–5.8 after one month. A higher kinetic rate of calcite also yields a minimum pH at 5.8 (Fig. S4). Liu and Maroto-Valer (2010) studied the pH stability of CO_2 -rock-brine systems where CO_2 was injected into brine with an initial pH of 2.6. The pH was buffered at 5.6 by Oriskany rock, which was mostly composed of quartz and calcite. Then, in the context of CAES, calcite would prevent aquifer acidification, albeit it is highly probable that the stored gas would change (O_2 decrease, CO_2 increase, etc.). This could be especially true for deeper aquifers with higher temperatures. The kinetic rates of minerals would be faster, the consumption of oxygen more rapid and the CO_2 content higher provided by present carbonates. Therefore, special attention should be paid to uncertainties in pyrite and calcite contents and their kinetic rate for any potential CAES facility.

The reservoir porosity has only slightly decreased in the present models, mostly due to the replacement of calcite by more voluminous gypsum. However, the estimated change is less than 0.9 % in the most realistic 2D-reservoir model. Hence, there is no significant risk for fluid transport.

These results are consistent with the simulation results of André et al. (2014); Todaka and Xu (2017). Conversely, calcite plays a role in the cementation of the sandstone rock matrix and a few percent of calcite dissolution might impact the rock's mechanical properties.

Only the complete oxidation of pyrite has been considered in our study due to the high oxygen gas content. But pyrite oxidation can be incomplete at lower O₂ concentrations, so forming elemental sulfur S₈ (Stuedel and Eckert, 2003), which might fill the pore volume and reduce the permeability of the reservoir (Shedid and Zekri, 2002). This might promote risks of formation damage. The formation of elemental sulfur can also sustain localized corrosion of steel well structures (Smith and Craig, 2005; Muschalle and Amro, 2013).

The on-going development of biomethane production, as an alternative to fossil fuels, will increase its proportion in natural gas infrastructures. Whereas O₂ concentration is very low in natural gas, coming from deep reduced hydrocarbon deposits, it can be up to 0.5 mol% in biomethane from a methanisation process (MARCOGAZ, 2022). The European Association for the Streamlining of Energy Exchange-gas (EASEE-gas) proposes to harmonize gas quality specifications in the Europe to ensure interoperability of the systems. With respect to O₂(g), a threshold of 0.001 mol% is recommended for underground storage facilities but concentrations up to 0.01 mol% are acceptable (EASEE-gas, 2005). Biomethane storage with the specification advised by EASEE-gas would have less impact on induced geochemical reactions in the reservoir than in our study. Nevertheless, phenomena occurring at low oxygen concentrations should be studied such as the potential formation of elemental sulfur discussed above.

6. Conclusions

An alternative cushion gas consisting of air partially depleted in O₂ was injected into an underground natural-gas reservoir, a deep aquifer located in the Paris Basin (France). The gas and groundwater were sampled at several wellbores, before and after air injection, to evaluate the induced geochemical reactions. Multiphase reactive transport models were developed using the HYTEC reactive transport code with an increasing complexity of the reservoir geometry, i.e. 0D-batch, 1D-radial and a more representative 2D-reservoir configuration.

The following conclusions can be drawn:

1. The reservoir is a carbonate-cemented sandstone composed by quartz, calcite, clay, feldspar and pyrite. The injected gas contained 8 mol% of O₂. About 6–9 months after injection completion, the gas analysis indicated a full depletion of O₂(g), meanwhile CO₂(g) was detected around 1.2–4 mol% (the CO₂(g) increased to 2–6 mol% 3 years after completion).
2. Water sampling showed that the initial pH value (7.5–8) became more acidic, around 6 and 3, after injection completion. The concentration of dissolved sulfates became quite high and the saturation index signaled an equilibrium with gypsum. After 3 years, the pH gradually returned back to the near-initial state and sulfates decreased by 2 to 3 times.
3. The batch model correctly reproduced the general gas-water-rock reactive sequence inferred from the literature and field data: 1/ full depletion of the injected O₂(g) due to pyrite oxidation, 2/ leading to acidity production and dissolved sulfates, 3/ the acidity is readily buffered by calcite dissolution in most cases, 4/ followed by gypsum precipitation and CO₂(g) exsolution. Oxidized Fe²⁺ from pyrite precipitated as goethite that might passivate pyrite dissolution in the long term (modeled in our study by a field factor applied to the reactive surface of the pyrite). The calculated changes in porosity were very small and would have an insignificant impact on the gas injectivity.
4. Pyrite kinetics had the most significant impact governing not only the amount of dissolved minerals, the consumption of O₂(g) and exsolution of CO₂(g), but also the spatial extent of these chemical reactions and, hence, the gas spreading inside the reservoir. An advective Damköhler

number was established for oxygen consumption due to pyrite oxidation in a multiphase system, Da_{I,O_2} . In the case of a fast kinetic rate, the multiphase reactive transport simulations demonstrated that O₂ was rapidly consumed in a quasi-constant radius of $Da_{I,O_2} \sim 1$. Mineral dissolution and the O₂(g) plume occurred only within this radius – located in the near-wellbore zone – until complete exhaustion of pyrite, following a zone-by-zone progressive depletion of the pyrite. When considering the field factor on pyrite oxidation, the gas-water-rock interactions changed in the whole spread of the injected gas (witnessed by the N₂(g) content).

5. Reactive transport makes a difference in modeling real natural systems, and having the field data was fundamental to adequately develop our multiphase reactive transport model. The representation of reservoir geometry was also important for modeling the structural trapping of gases and, accordingly, the adequate physics of the overall gas-water-rock interactions.

The field and modeling results presented in this study could also be used as a workflow for other gas storage facilities such as for biomethane, CAES, and CO₂. Since there is some possibility of strong acidification and changes in gas composition when injecting 8 mol% of oxygen, special attention should then be paid to uncertainties in pyrite and calcite contents and their kinetic rate for any potential CAES facility. With regard to biomethane storage, when calcite is homogeneously present in the rock-forming reservoir, it can be expected from the present study that the reactivity of oxygen injected according to the EASEE-gas specification quality would probably have a low impact on gas composition, reservoir geochemistry and gas injectivity. Nevertheless, a heterogeneous distribution of calcite could also lead to locally low acidic pH. Furthermore, additional geochemical processes occurring at low oxygen concentrations should then be implemented in the models, such as the potential formation of elemental sulfur and associated risks.

Our study focused on the immediate effects of air injection into the reservoir. Further modeling studies based on the field data acquired on the UGS reservoir are on-going to provide an insight into the long-term evolution of the groundwater and its progressive return to the initial background state.

CRedit authorship contribution statement

Irina Sin: Conceptualization, Methodology, Software, Validation, Formal analysis, Investigation, Writing – original draft, Writing – review & editing, Visualization. **Laurent De Windt:** Conceptualization, Methodology, Validation, Formal analysis, Investigation, Writing – original draft, Writing – review & editing, Visualization. **Camille Banc:** Formal analysis, Writing – original draft. **Patrick Goblet:** Methodology, Formal analysis. **David Dequid:** Conceptualization, Validation, Resources, Writing – review & editing.

Data availability

Data will be made available on request.

Declaration of competing interest

The authors declare that they have no known competing financial interests or personal relationships that could have appeared to influence the work reported in this paper.

Acknowledgments

Storengy and Mines Paris - PSL are gratefully thanked for funding this study. Storengy is thanked for providing the field data reported in this study.

The authors greatly acknowledge the former colleagues from Ecole des Mines de Paris, Anne Bariteau and Jean-Michel Schmitt, for their very valuable work in 1996 on the geochemical investigations and modeling of the UGS site.

The authors gratefully acknowledge the PGT reactive transport consortium (Pôle Géochimie-Transport), a national research framework that supports the developments, tests and validation of HYTEC models.

We gratefully acknowledge the reviewers for their extensive reviews and relevant comments that greatly helped to increase the clarity and quality of the paper.

Appendix A. Supplementary data

Supplementary data to this article can be found online at <https://doi.org/10.1016/j.scitotenv.2023.161657>.

References

- André, L., Azaroual, M., Bernstone, C., Wittek, A., 2014. Modeling the geochemical impact of an injection of CO₂ and associated reactive impurities SO₂ and O₂ into a saline reservoir. *Transp. Porous Media* 108, 185–205. <https://doi.org/10.1007/s11242-014-0359-7> URL: 10.1007/s11242-014-0359-7.
- Bauer, S., Class, H., Ebert, M., Feeser, V., Götz, H., Holzheid, A., Kolditz, O., Rosenbaum, S., Rabbel, W., Schäfer, D., Dahmke, A., 2012. Modeling, parameterization and evaluation of monitoring methods for CO₂ storage in deep saline formations: the CO₂-MoPa project. *Environ. Earth Sci.* 67, 351–367. <https://doi.org/10.1007/s12665-012-1707-y> URL: 10.1007/s12665-012-1707-y.
- Berta, M., Dethlefsen, F., Ebert, M., Gundske, K., Dahmke, A., 2016. Surface passivation model explains pyrite oxidation kinetics in column experiments with up to 11 bars p(O₂). *Environ. Earth Sci.* 75, 1–13.
- Berta, M., Ebert, M., Schäfer, D., Dethlefsen, F., 2017. Experimental process parameterization of a 3D site-scale model on effects of a compressed air intrusion into a shallow aquifer. *Energy Procedia* 125. European Geosciences Union General Assembly 2017, EGU Division Energy, Resources & Environment (ERE), pp. 622–629. <https://doi.org/10.1016/j.egypro.2017.08.250>. <https://www.sciencedirect.com/science/article/pii/S1876610217337566>.
- Bourg, I.C., Beckingham, L.E., DePaolo, D.J., 2015. The nanoscale basis of CO₂ trapping for geologic storage. *Environ. Sci. Technol.* 49, 10265–10284.
- Brantley, S.L., Kubicki, J.D., White, A.F., et al., 2008. *Kinetics of Water-rock Interaction*. vol. 168. Springer.
- Brooks, R., Corey, A., 1964. Hydraulic properties of porous media. *Hydrology Papers*. Colorado State University.
- Bui, H., Herzog, R., Jacewicz, D., Lange, G., Scarpace, E., Thomas, H., 1990. *Compressed-air Energy Storage: Pittsfield Aquifer Field Test*. Technical Report. Electric Power Research Inst., Palo Alto, CA (USA) ANR Storage Co., Detroit.
- Carrayrou, J., Hoffmann, J., Knabner, P., Kräutle, S., De Dieuleveult, C., Erhel, J., van der Lee, J., Lagneau, V., Mayer, K.U., Macquarrie, K.T., 2010. Comparison of numerical methods for simulating strongly nonlinear and heterogeneous reactive transport problems — the MoMaS benchmark case. *Comput. Geosci.* 14, 483–502.
- Chabab, S., Ahmadi, P., Théveneau, P., Coquelet, C., Chapoy, A., Corvisier, J., Paricaud, P., 2020a. Measurements and modeling of high-pressure O₂ and CO₂ solubility in brine (H₂O + NaCl) between 303 and 373 K and pressures up to 36 MPa. *J. Chem. Eng. Data* 66, 609–620.
- Chabab, S., Théveneau, P., Coquelet, C., Corvisier, J., Paricaud, P., 2020b. Measurements and predictive models of high-pressure H₂ solubility in brine (H₂O + NaCl) for underground hydrogen storage application. *Int. J. Hydrog. Energy* 45, 32206–32220. <https://doi.org/10.1016/j.ijhydene.2020.08.192>. <https://www.sciencedirect.com/science/article/pii/S0304386X22000585>.
- Collet, A., Regnault, O., Ozhigin, A., Imantayeva, A., Garnier, L., 2022. Three-dimensional reactive transport simulation of Uranium in situ recovery: large-scale well field applications in Shu Saryssu Basin, Tortkuduk deposit (Kazakhstan). *Hydrometallurgy*, 105873 <https://doi.org/10.1016/j.hydromet.2022.105873> URL: <https://www.sciencedirect.com/science/article/pii/S0304386X22000585>.
- Corvisier, J., Bonvalot, A., Lagneau, V., Chiquet, P., Renard, S., Sterpenich, J., Pironon, J., 2013. Impact of co-injected gases on CO₂ storage sites: geochemical modeling of experimental results. *Proceedings of the International Conference on Greenhouse Gas Technology 11*, Kyoto, *Energy Procedia*, pp. 3699–3710.
- De Windt, L., Marsal, F., Corvisier, J., Pellegrini, D., 2014. Modeling of oxygen gas diffusion and consumption during the oxidic transient in a disposal cell of radioactive waste. *Appl. Geochem.* 41, 115–127.
- De Windt, L., Spycher, N.F., 2019. Reactive transport modeling: a key performance assessment tool for the geologic disposal of nuclear waste. *Elements* 15, 99–102.
- Dethlefsen, F., Nolde, M., Schäfer, D., Dahmke, A., 2017. Basic parameterization of Schleswig-Holstein's shallow geological formations for numerical reactive transport simulations: representative groundwater compositions. *Environ. Earth Sci.* 76, 59. <https://doi.org/10.1007/s12665-016-6343-5> URL: <http://link.springer.com/10.1007/s12665-016-6343-5>.
- EASEE-gas, 2005. Common business practice 2005-001/02 2005. URL https://easee-gas.eu/download_file/DownloadFile/4/cbp-2005-001-02-harmonisation-of-natural-gas-quality/.
- Evangelou, V.P.B., Zhang, Y.L., 1995. A review: pyrite oxidation mechanisms and acid mine drainage prevention. *Crit. Rev. Environ. Sci. Technol.* 25, 141–199. <https://doi.org/10.1080/10643389509388477> URL: doi:10.1080/10643389509388477, doi:10.1080/10643389509388477. publisher: Taylor & Francis_eprint.
- Gombert, P., Ghoreychi, M., 2018. *Historique et panorama des stockages souterrains actuels en France et dans le monde*. *Géologues* 196, 4–9 URL: <https://hal-ineris.archives-ouvertes.fr/ineris-03318097>. publisher: Société Géologique de France.
- Grise, S., Saldanha, B., 2008. Effects of oxygen, temperature and salinity on carbon steel corrosion in aqueous solutions; model predictions versus laboratory results. *CORROSION* 2008. OnePetro.
- Guo, C., Li, C., Zhang, K., Cai, Z., Ma, T., Maggi, F., Gan, Y., El-Zein, A., Pan, Z., Shen, L., 2021. The promise and challenges of utility-scale compressed air energy storage in aquifers. *Appl. Energy* 286, 116513. <https://doi.org/10.1016/j.apenergy.2021.116513>. <https://www.sciencedirect.com/science/article/pii/S0306261921000714>.
- Haddad, P.G., Mura, J., Castéran, F., Guignard, M., Ranchou-Peyruse, M., Sénéchal, P., Larregieu, M., Isaure, M.P., Svahn, I., Moonen, P., et al., 2022. Biological, geological and chemical effects of oxygen injection in underground gas storage aquifers in the setting of biomethane deployment. *Sci. Total Environ.* 806, 150690.
- Hajiw, M., Corvisier, J., El Ahmar, E., Coquelet, C., 2018. Impact of impurities on CO₂ storage in saline aquifers: modelling of gases solubility in water. *Int. J. Greenh. Gas Control* 68, 247–255.
- Helgeson, H.C., 1969. Thermodynamics of hydrothermal systems at elevated temperatures and pressures. *Am. J. Sci.* 267, 729–804.
- Huertas, F.J., Chou, L., Wollast, R., 1999. Mechanism of kaolinite dissolution at room temperature and pressure part II: kinetic study. *Geochim. Cosmochim. Acta* 63, 3261–3275.
- Huminicki, D.M., Rimstidt, J.D., 2009. Iron oxyhydroxide coating of pyrite for acid mine drainage control. *Appl. Geochem.* 24, 1626–1634. <https://doi.org/10.1016/j.apgeochem.2009.04.032>. <https://www.sciencedirect.com/science/article/pii/S0883292709001401>.
- Ilojesi, C.O., Beckingham, L.E., 2021a. Assessment of geochemical limitations to utilizing CO₂ as a cushion gas in compressed energy storage systems. *Environ. Eng. Sci.* 38, 115–126. <https://doi.org/10.1089/ees.2020.0345>. <https://www.liebertpub.com/doi/10.1089/ees.2020.0345>.
- Ilojesi, C.O., Beckingham, L.E., 2021b. Influence of storage period on the geochemical evolution of a compressed energy storage system. *Front. Water* 3. <https://www.frontiersin.org/article/10.3389/frwa.2021.689404>.
- Juez-Larré, J., Gessel, S.v., Dalman, R., Remmelts, G., Groenenberg, R., 2019. Assessment of underground energy storage potential to support the energy transition in the Netherlands. *First Break* 37, 57–66 URL: <https://www.earthdoc.org/content/journals/10.3997/1365-2397.n0039>, doi:10.3997/1365-2397.n0039. publisher: European Association of Geoscientists & Engineers.
- Jung, H.B., Um, W., Cantrell, K.J., 2013. Effect of oxygen co-injected with carbon dioxide on gothic shale caprock-CO₂-brine interaction during geologic carbon sequestration. *Chem. Geol.* 354, 1–14.
- Klein, E., De Lucia, M., Kempka, T., Kühn, M., 2013. Evaluation of long-term mineral trapping at the Ketzin pilot site for CO₂ storage: an integrative approach using geochemical modeling and reservoir simulation. *Int. J. Greenh. Gas Control* 19, 720–730.
- Köhler, S.J., Dufaud, F., Oelkers, E.H., 2003. An experimental study of illite dissolution kinetics as a function of pH from 1.4 to 12.4 and temperature from 5 to 50 C. *Geochim. Cosmochim. Acta* 67, 3583–3594.
- Lagneau, V., Regnault, O., Descostes, M., 2019. Industrial deployment of reactive transport simulation: an application to uranium in situ recovery. Chapter 11n: *Druhan Tournassat, J. (Ed.) Mineralogical Society of America ed.. Reviews in Mineralogy and Geochemistry* 85. *Reactive Transport in Natural And Engineered Systems*, pp. 499–528. <https://doi.org/10.2138/rmg.2019.85.16>.
- Laille, J., Molinar, J., Wents, A., 1988. Inert gas injection as part of the cushion of the underground storage of Saint-Clair-Sur-Epte, France. *All Days. SPE* <https://doi.org/10.2118/17740-ms> URL: <https://www.sciencedirect.com/science/article/pii/S0304386X22000585>.
- Lasaga, A.C., 1984. Chemical kinetics of water-rock interactions. *J. Geophys. Res. Solid Earth* 1978–2012 (89), 4009–4025.
- van der Lee, J., 2009. *Thermodynamic And Mathematical Concepts of CHESSE*. École des Mines de Paris, Centre de Géosciences, Fontainebleau, France.
- van der Lee, J., de Windt, L., Lagneau, V., Goblet, P., 2003. Module-oriented modeling of reactive transport with HYTEC. *Comput. Geosci.* 29, 265–275.
- Lemmon, E.W., Huber, M.L., McLinder, M.O., 2013. NIST Reference Database 23: Reference Fluid Thermodynamic And Transport Properties-REFPROP, Version 9.1. National Institute of Standards and Technology, Standard Reference Data Program.
- Lichtner, P., 1996. Continuum formulation of multicomponent-multiphase reactive transport. In: *Lichtner, P., Steefel, C., Oelkers, E. (Eds.), Reactive Transport in Porous Media*. *Reviews in Mineralogy*, 34, pp. 1–81 Chapter 1.
- Liu, Q., Maroto-Valer, M.M., 2010. Investigation of the pH effect of a typical host rock and buffer solution on CO₂ sequestration in synthetic brines. *Fuel Process. Technol.* 91, 1321–1329. <https://doi.org/10.1016/j.fuproc.2010.05.002>. <https://www.sciencedirect.com/science/article/pii/S0378382010001402>.
- MARCOGAZ, 2022. *Biomethane Acceptance in Underground Gas Storage Facilities*. Technical Report.
- Martin, R.L., 2002. Corrosion consequences of oxygen entry into oilfield brines. *CORROSION* 2002. OnePetro URL: <http://link.springer.com/10.1007/s12665-016-6343-5>.
- Marty, N.C., Claret, F., Lassin, A., Tremosa, J., Blanc, P., Madé, B., Giffaut, E., Cochepin, B., Tournassat, C., 2015. A database of dissolution and precipitation rates for clay-rocks minerals. *Appl. Geochem.* 55, 108–118.
- Marty, N.C., Lach, A., Lerouge, S., Claret, F., Fauchet, C., Madé, B., Lundy, M., Lagroix, F., Tournassat, C., 2018. Weathering of an argillaceous rock in the presence of atmospheric conditions: a flow-through experiment and modelling study. *Appl. Geochem.* 96, 252–263.
- Matos, C.R., Carneiro, J.F., Silva, P.P., 2019. Overview of large-scale underground energy storage technologies for integration of renewable energies and criteria for reservoir identification. *J. Energy Storage* 21, 241–258.
- McCain Jr., W., 1991. Reservoir-fluid property correlations-state of the art. *SPE Reserv. Eng.* 6, 266–272.
- Metz, B., Davidson, O., De Coninck, H., Loos, M., Meyer, L., 2005. *IPCC Special Report on Carbon Dioxide Capture And Storage*. Cambridge University Press, Cambridge.
- Michelsen, M.L., Møllerup, J., 2007. *Thermodynamic Models: Fundamentals & Computational Aspects*. 2nd ed. Tie-Line Publications, Denmark.

- Mouli-Castillo, J., Heinemann, N., Edlmann, K., 2021. Mapping geological hydrogen storage capacity and regional heating demands: An applied UK case study. *Appl. Energy* 283, 116348. <https://doi.org/10.1016/j.apenergy.2020.116348>. <https://www.sciencedirect.com/science/article/pii/S030626192031730X>.
- Muschalle, T., Amro, M., 2013. Influence of Oxygen Impurities on Underground Gas Storage And Surface Equipment. Literature Study. Technical Report. DGMK.
- Nazeri, M., Chapoy, A., Burgass, R., Tohidi, B., 2017. Measured densities and derived thermodynamic properties of CO₂-rich mixtures in gas, liquid and supercritical phases from 273 K to 423 K and pressures up to 126 MPa. *J. Chem. Thermodyn.* 111, 157–172.
- Nicholson, R.V., Gillham, R.W., Reardon, E.J., 1988. Pyrite oxidation in carbonate-buffered solution: 1. experimental kinetics. *Geochim. Cosmochim. Acta* 52, 1077–1085.
- Nicholson, R.V., Gillham, R.W., Reardon, E.J., 1990. Pyrite oxidation in carbonate-buffered solution: 2. rate control by oxide coatings. *Geochim. Cosmochim. Acta* 54, 395–402.
- Palandri, J.L., Kharaka, Y.K., 2004. A Compilation of Rate Parameters of Water-mineral Interaction Kinetics for Application to Geochemical Modeling. Technical Report. Geological Survey, Menlo Park, CA.
- Pearce, J.K., Brink, F., Dawson, G.W., Poitras, J., Southam, G., Paterson, D.J., Wolhuter, A., Underschultz, J.R., 2022. Core characterisation and predicted CO₂ reactivity of sandstones and mudstones from an Australian oil field. *Int. J. Coal Geol.* 250, 103911. <https://doi.org/10.1016/j.coal.2021.103911>. <https://www.sciencedirect.com/science/article/pii/S016651622100238X>.
- Pearce, J.K., Golab, A., Dawson, G.K., Knuefing, L., Goodwin, C., Golding, S.D., 2016. Mineralogical controls on porosity and water chemistry during O₂-SO₂-CO₂ reaction of CO₂ storage reservoir and cap-rock core. *Appl. Geochem.* 75, 152–168.
- Pérez-López, R., Cama, J., Miguel Nieto, J., Ayora, C., Saaltink, M.W., 2009. Attenuation of pyrite oxidation with a fly ash pre-barrier: reactive transport modelling of column experiments. *Appl. Geochem.* 24, 1712–1723. <https://doi.org/10.1016/j.apgeochem.2009.05.001>. <https://www.sciencedirect.com/science/article/pii/S0883292709001565>.
- Plummer, L., Wigley, T., Parkhurst, D., 1978. The kinetics of calcite dissolution in CO₂-water systems at 5 degrees to 60 degrees C and 0.0 to 1.0 atm CO₂. *Am. J. Sci.* 278, 179–216.
- Rimstidt, J.D., Vaughan, D.J., 2003. Pyrite oxidation: a state-of-the-art assessment of the reaction mechanism. *Geochim. Cosmochim. Acta* 67, 873–880.
- Robinson, D.B., Peng, D.Y., 1978. The Characterization of the Heptanes And Heavier Fractions for the GPA Peng-Robinson Programs. Technical Report.
- Schmitt, J., Goblet, P., Bariteau, A., 1996. Étude du phénomène de consommation d'oxygène dans le stockage souterrain de Saint-Illiers. Technical Report. École des Mines de Paris, Fontainebleau.
- Schutt, H.U., Lyle, F.F., 1998. CO₂/H₂S corrosion under wet gas pipeline conditions in the presence of bicarbonate, chloride, and oxygen. *CORROSION* 98. OnePetro.
- Seigneur, N., Kangni-Foli, E., Lagneau, V., Dauzères, A., Poyet, S., Le Bescop, P., L'Hôpital, E., de Lacallierie, J.B.d., 2020. Predicting the atmospheric carbonation of cementitious materials using fully coupled two-phase reactive transport modelling. *Cem. Concr. Res.* 130, 105966.
- Shedid, S.A., Zekri, A.Y., 2002. Formation damage due to sulfur deposition in porous media. International Symposium And Exhibition on Formation Damage Control. OnePetro.
- Sin, I., 2015. Numerical simulation of compressible two-phase flow and reactive transport in porous media. Applications to the Study of CO₂ Storage And Natural Gas Reservoirs. Ph. D. thesis. MINES ParisTech. <https://pastel.archives-ouvertes.fr/tel-01306860/document>.
- Sin, I., Corvisier, J., 2019. Multiphase multicomponent reactive transport and flow modeling. Mineralogical Society of America edn: Druhan, J., Tourmassat, C. (Eds.), *Reactive Transport in Natural And Engineered Systems. Reviews in Mineralogy And Geochemistry* 85, pp. 143–195. <https://doi.org/10.2138/rmg.2019.85.6> Chapter 6.
- Sin, I., Lagneau, V., Corvisier, J., 2017. Integrating a compressible multicomponent two-phase flow into an existing reactive transport simulator. *Adv. Water Resour.* 100, 62–77. <https://doi.org/10.1016/j.advwatres.2016.11.014>. <http://www.sciencedirect.com/science/article/pii/S0309170816307060>.
- Sjöberg, E.L., Rickard, D.T., 1984. Temperature dependence of calcite dissolution kinetics between 1 and 62 C at pH 2.7 to 8.4 in aqueous solutions. *Geochim. Cosmochim. Acta* 48, 485–493.
- Smith, L., Craig, B.D., 2005. Practical corrosion control measures for elemental sulfur containing environments. *CORROSION* 2005. OnePetro.
- Steeffel, C., Appelo, C.A.J., Arora, B., Jacques, D., Kalbacher, T., Kolditz, O., Lagneau, V., Lichtner, P., Mayer, K., Meeussen, J.C.L., 2014. Reactive transport codes for subsurface environmental simulation. *Comput. Geosci.* 1–34. <https://doi.org/10.1007/s10596-014-9443-x>.
- Steeffel, C.I., 2008. *Geochemical kinetics and transport. Kinetics of Water-rock Interaction.* Springer, pp. 545–589.
- Steel, L., Mackay, E., Maroto-Valer, M.M., 2018. Experimental investigation of CO₂-brine-calcite interactions under reservoir conditions. *Fuel Process. Technol.* 169, 122–131. <https://doi.org/10.1016/j.fuproc.2017.09.028>. <https://www.sciencedirect.com/science/article/pii/S037838201731127X>.
- Steucler, R., Eckert, B., 2003. Solid sulfur allotropes. *Elemental Sulfur And Sulfur-rich Compounds. I*, pp. 1–80.
- Succar, S., Williams, R.H., et al., 2008. Compressed air energy storage: theory, resources, and applications for wind power. Princeton Environmental Institute Report 8. 81.
- Swoboda-Colberg, N.G., Drever, J.I., 1993. Mineral dissolution rates in plot-scale field and laboratory experiments. *Chem. Geol.* 105, 51–69.
- Todaka, N., Xu, T., 2017. Reactive transport simulation to assess geochemical impact of impurities on CO₂ injection into siliciclastic reservoir at the Otway site, Australia. *Int. J. Greenh. Gas Control* 66, 177–189.
- Vu, H.P., Black, J.R., Haese, R.R., 2018. The geochemical effects of O₂ and SO₂ as CO₂ impurities on fluid-rock reactions in a CO₂ storage reservoir. *Int. J. Greenh. Gas Control* 68, 86–98. <https://doi.org/10.1016/j.ijggc.2017.11.001>.
- Wang, B., Bauer, S., 2019. Induced geochemical reactions by compressed air energy storage in a porous formation in the North German Basin. *Appl. Geochem.* 102, 171–185. <https://doi.org/10.1016/j.apgeochem.2019.02.003>. <https://www.sciencedirect.com/science/article/pii/S0883292719300290>.
- Wang, Y., Zhang, L., Soong, Y., Dilmore, R., Liu, H., Lei, H., Li, X., 2019. From core-scale experiment to reservoir-scale modeling: a scale-up approach to investigate reaction-induced permeability evolution of CO₂ storage reservoir and caprock at U.S. CO₂ storage site. *Comput. Geosci.* 125, 55–68. <https://doi.org/10.1016/j.cageo.2019.01.006>. <https://www.sciencedirect.com/science/article/pii/S00983300418308653>.
- Wei, N., Li, X., Wang, Y., Zhu, Q., Liu, S., Liu, N., Su, X., 2015. Geochemical impact of aquifer storage for impure CO₂ containing O₂ and N₂: Tongliao field experiment. *Appl. Energy* 145, 198–210.
- Welch, V., Dann, M., Mehta, B., 1990. Predicting oxygen depletion in reservoir environments. SPE Annual Technical Conference And Exhibition. OnePetro.
- White, A.F., 2008. Quantitative approaches to characterizing natural chemical weathering rates. *Kinetics of Water-rock Interaction.* Springer, pp. 469–543.
- White, A.F., Brantley, S.L., 2003. The effect of time on the weathering of silicate minerals: why do weathering rates differ in the laboratory and field? *Chem. Geol.* 202, 479–506.
- Williamson, M.A., Rimstidt, J.D., 1994. The kinetics and electrochemical rate-determining step of aqueous pyrite oxidation. *Geochim. Cosmochim. Acta* 58, 5443–5454.
- Wolery, T., Sutton, M., 2013. Evaluation of Thermodynamic Data. Technical Report 640133. Lawrence Livermore National Laboratory (LLNL), Livermore, CA, USA.